International Journal of Biological Macromolecules 261 (2024) 129758

Contents lists available at ScienceDirect

International Journal of Biological Macromolecules

journal homepage: www.elsevier.com/locate/ijbiomac

Receptor mediated targeting of EGF-conjugated alginate-PAMAM nanoparticles to lung adenocarcinoma: 2D/3D *in vitro* and *in vivo* evaluation

Esra Ilhan-Ayisigi [a,b], Pelin Saglam-Metiner [b,c], Ebru Sanci [d], Buket Bakan [e], Yeliz Yildirim [f], Aylin Buhur [g], Altug Yavasoglu [g], N. Ulku Karabay Yavasoglu [c,d,h,*], Ozlem Yesil-Celiktas [b,c,**]

[a] Department of Genetic and Bioengineering, Faculty of Engineering and Architecture, Kirsehir Ahi Evran University, Kirsehir, Turkey
[b] Department of Bioengineering, Faculty of Engineering, Ege University, Izmir, Turkey
[c] Translational Pulmonary Research Center (EgeSAM), Ege University, Izmir, Turkey
[d] Center for Drug Research and Pharmacokinetic Applications (ARGEFAR), Ege University, Izmir, Turkey
[e] Department of Molecular Biology and Genetics, Faculty of Science, Ataturk University, Erzurum, Turkey
[f] Department of Chemistry, Faculty of Science, Ege University, Izmir, Turkey
[g] Department of Histology and Embryology, Faculty of Medicine, Ege University, Izmir, Turkey
[h] Department of Biology, Faculty of Science, Ege University, Izmir, Turkey

ARTICLE INFO

Keywords:
Alginate
PAMAM dendrimer
Microfluidic synthesis
Carboplatin
Targeted drug delivery
In vivo lung cancer model

ABSTRACT

Carboplatin (cis-diamine (1,1-cyclobutandicarboxylaso)-platinum (II)) is a second-generation antineoplastic drug, which is widely used for chemotherapy of lung, colon, breast, cervix, testicular and digestive system cancers. Although preferred over cisplatin due to the lower incidence of nephrotoxicity and ototoxicity, efficient carboplatin delivery remains as a major challenge. In this study, carboplatin loaded alginate- poly(amidoamine) (PAMAM) hybrid nanoparticles (CAPs) with mean sizes of 192.13 ± 4.15 nm were synthesized using a microfluidic platform, then EGF was conjugated to the surface of CAPs (EGF-CAPs) for the receptor-targeted delivery. Hence, increased $FITC^{+}$ cell counts were observed in A549 spheroids after EGF-CAP treatment compared to CAP in the 3D cellular uptake study. As such, the cytotoxicity of EGF-CAP was approximately 2-fold higher with an IC_{50} value of 35.89 ± 10.37 μg/mL compared to the CAPs in A549 spheroids. Based on *in vivo* experimental animal model, anti-tumor activities of the group treated with CAP decreased by 61 %, whereas the group treated with EGF-CAP completely recovered. Additionally, EGF-CAP application was shown to induce apoptotic cell death. Our study provided a new strategy for designing a hybrid nanoparticle for EGFR targeted carboplatin delivery with improved efficacy both *in vitro* and *in vivo* applications.

1. Introduction

In recent years, clinical and preclinical applications of nanoparticles (NPs) have been widespread, to navigate systemic, microenvironmental and cellular biological barriers and offer the benefits of reduced toxicity and enhanced efficacy compared to the 'free' drug [1]. Indeed, these nanoparticles have the potential to improve drug solubility and stability, eliminate drug aggregation and prolong circulation times to enhance safety and efficacy [2,3]. The synthesis of nanoparticles by microfluidics permits fast handling, small component requirements for the process, and a well-controlled microenvironment [4]. Alginate is a naturally occurring algal polysaccharide suitable to form the shell of the nanoparticles synthesized with microfluidic platforms due to simple gelation properties in divalent cations such as calcium (II) [5]. However, the primary disadvantages of alginate/divalent ion-based nanogel systems are the lack of stability and dissociation because of the rapid exchange of calcium (II) cations with other cations under physiological conditions [6,7]. Thus, their utility as delivery vehicles for nanomedicine requires a second component to interact with alginate. PAMAM dendrimers with higher surface functional group density compared to conventional macromolecules are ideal for this purpose, which in parallel can enhance the solubility of hydrophobic drugs [8]. Moreover, PAMAMs can be modified by polyethylene glycols, aptamers, antibodies to direct drugs to specific tissues and reduce the devastating

* Correspondence to: U. K. Yavasoglu, Department of Biology, Faculty of Science, Ege University, Izmir, Turkey.
** Correspondence to: O. Yesil-Celiktas, Department of Bioengineering, Faculty of Engineering, Ege University, Izmir, Turkey.
E-mail addresses: ulku.karabay@ege.edu.tr (N.U.K. Yavasoglu), ozlem.yesil.celiktas@ege.edu.tr (O. Yesil-Celiktas).

https://doi.org/10.1016/j.ijbiomac.2024.129758
Received 27 September 2023; Received in revised form 6 January 2024; Accepted 24 January 2024
Available online 28 January 2024

side effects, which is even more critical in cancer treatments. Epidermal growth factor receptor (EGFR), is the first discovered receptor of tyrosine kinases of the ErbB family. The increased EGFR levels correlate with poor prognosis in several types of epithelial cancers including non-small cell lung cancer (NSCLC) [9,10]. Among cancer-mediated pathways, tyrosine kinases play important roles in regulating cell signalling, and activated tyrosine kinases can increase tumor cell growth, proliferation, anti-apoptotic induction, and induce metastasis [11]. In the last decade, several anti-EGFR treatment strategies including receptor-blocking monoclonal antibodies (such as cetuximab, panitumumab) or small molecule tyrosine kinase inhibitors (such as erlotinib, gefitinib) have been clinically approved [12]. As of 2022, 114 mAb products have been approved by the European Medicines Agency and US Food and Drug Administration (excluding biosimilar products and Fc-fusion proteins), and 11 of these mAbs are directed to tumor cell surface tyrosine kinase receptors involved in survival and proliferation pathways such as HER2, EGFR, PDGFRα [13]. In parallel to EGFR-inhibition therapies, potential applications of various EGFR-targeted nanoparticles in *in vitro* [14–18] and preclinical *in vivo* models [16–19] have shown promising results to achieve tumor cell-specific drug delivery and internalization. Although various EGFR-specific targeting ligands such as antibodies [20], antibody fragments [21,22], recombinant epidermal growth factor [16,23–28], specific peptides [29,30] and aptamers [31] have been developed to target EGFR through the functionalization of nanoparticle surface, the use of native ligand epidermal growth factor (EGF) holds promise for further anticancer nanomedicine strategy. The endogenous ligand, EGF, is significantly smaller than both antibodies and fragments and has a high binding affinity due to the low dissociation constant with respect to EGFR, providing a unique target for anti-cancer drug applications [12,32]. In this study, we hypothesized that EGF conjugated alginate-PAMAM hybrid nanoparticles loaded with carboplatin (EGF-CAPs), could bind with EGFR due to the presence of the specific EGF ligand on the EGF-CAPs surface. The binding of EGF on the EGF-CAPs surface with EGFR overexpressed on the surface of NSCLC cells could induce receptor-mediated endocytosis leading to an increase of cellular uptake of nanoparticles and reduce the proliferation of cancer cells. Thus, EGF conjugation was achieved *via* carbodiimide chemistry following the microfluidic synthesis of CAPs, then the therapeutic potential of EGF-CAPs were evaluated in 2D *in vitro* culture as well as 3D spheroid culture and correlated to the antitumorigenic activities in *in vivo*.

2. Material and methods

2.1. Materials

EGF (Recombinant Human Epidermal Growth Factor, Gibco™) and EGF ELISA Kit (EGF Human Instant ELISA™ Kit, Invitrogen) were purchased from ThermoFisher-Scientific, while alginic acid sodium salt from brown algae (alginate), Polyamidoamine (PAMAM) dendrimer (ethylenediamine core, generation 4.0, G4) solution, N-(3-dimethylaminopropyl)-N′-ethylcarbodiimide hydrochloride (EDC), N-hydroxysulfosuccinimide sodium salt (NHS) and all other chemicals were obtained from Sigma-Aldrich. Carboplatin (150 mg/15 mL vial) was obtained from Kocak Farma, Turkey. All cell culture reagents, Trypan blue dye, MTT (3-(4,5-dimethylthiazol-2-yl)-2,5-diphenyltetrazolium bromide) and dimethyl sulfoxide (DMSO) were purchased from Sigma-Aldrich (USA), live/dead cell staining kit was purchased from Molecular Probes, Invitrogen (USA). Promega DeadEnd™ Colorimetric Apoptosis Detection System (TUNEL, Promega Corp. Madison, USA, Cat No: G7130), and Biotinylated secondary antibody and streptavidin conjugated horse radish peroxidase (Thermo Scientific Cas no: 85–9043) were purchased from Zymed Laboratories. All chemicals used in the *in vivo* experiment were of analytical grade.

2.2. Synthesis of alginate-PAMAM hybrid nanoparticles

Firstly, the activation of alginate polymer has been carried out by adding EDC (0.1 mmol) and NHS (0.05 mmol) reagents into 1 mL of aqueous alginate (20 mg/mL) solution and mixing for 2 h in the dark. The aliquot volume of carboplatin stock solution at 10 mg/mL concentration was added to activated alginate, mixed and transferred to the 1 mL plastic syringe then pumped through the central channel (PFA Tubing 1/16" O.D. x .010", Idex Health & Science) of a metal microfluidic system (0.25 mm I.D. four lines connected crosses from VICI Valco Instruments Co. Inc.) by a syringe pump (New Era Pump Systems Inc.). The final carboplatin concentration at the outlet of the microfluidic chip was set to 20 μg/mL and the initial carboplatin concentration requirement in the syringe was calculated separately for each flow rate ratio (FRR) depending on the dilution rate through the microfluidic synthesis. The continuous production of carboplatin-loaded (CAP) or empty (AP) alginate- PAMAM hybrid nanoparticles was achieved by pumping two aqueous PAMAM dendrimer solutions (at concentrations of 0.04 mM or 0.08 mM) through the lateral inlets of the microfluidic system and hydrodynamically focusing the central activated alginate solution. For synthesis of AP alginate solution did not contain carboplatin in the syringe. While the central stream of alginate (20 mg/mL) was pumped at a rate of 10 μL/min, PAMAM aqueous solutions were pumped from the side streams at different flow rates of 200, 300 and 400 μL/min. Thus, the employed flow rate ratios, which is the ratio of the flow rates of the side streams to that of the central stream, were studied as 40, 60 and 80, respectively. CAP and AP nanoparticle solutions were collected from the output channel and centrifuged at 8750*g* (9000 rpm) (Eppendorf MiniSpin® plus). The pellet was washed two times *via* dispersion in deionized water and centrifuged again to remove the residues. The remaining nanoparticle dispersions were lyophilized. Supernatant of CAP nanoparticles was analyzed to determine encapsulation efficiency.

2.3. Characterization of alginate-PAMAM hybrid nanoparticles

Size distributions, polydispersity indexes (PDI) and zeta potential values of synthesized alginate-PAMAM hybrid nanoparticles were measured with the Malvern Zetasizer device (Nano-ZS, Malvern Inst. Ltd., UK). The molecular structures were determined by FTIR (Fourier Transform Infrared Spectroscopy) and XPS (X-ray Photoelectron Spectroscopy). FTIR spectra of alginate polymer, alginate- PAMAM hybrid nanoparticles were determined by PerkinElmer Spectrum 100 instrument between the wavelengths of 400–4000 cm^{-1}. XPS analysis was carried out by Thermo Scientific K-Alpha device using the Al Kα monochromatic X-ray source (1486.68 eV) and 300 μm X-ray spot sizes. SEM (Scanning Electron Microscopy) and DSC (Differential Scanning Calorimeter) analyses were performed to study the surface morphology and thermal characterizations, respectively. The nanoparticles were coated with 10 nm gold-palladium under vacuum at Leica EM ACE600 sputter-coater and the SEM photographs were taken by FEG SEM (Thermo Scientific, Apreo S, Netherlands). The DSC system (TA Instruments, Q20) was flushed with pure dry nitrogen at a flow rate of 5 mL/min and samples (5 mg) were analyzed at temperature range of 20–350 °C with a heating rate of 10 °C/min. The separated supernatant from the microchip was analyzed by high performance liquid chromatography (HPLC) (Shimadzu LC-20A PDA) to determine the unencapsulated carboplatin concentration. Samples filtered through a 0.45 μm filter were pumped to an ACE C18 column (250 mm × 4.6 mm × 5 μm in size). The mobile phase was prepared at a concentration of 20 mM PBS buffer (75 %) as the aqueous phase and acetonitrile (25 %) as the organic phase. The flow rate of the mobile phase was adjusted to 1 mL/min and the samples were injected into the system with an injection volume of 20 μL, while the injection time was 10 min (35 °C) and the detection wavelength was 227 nm. Encapsulation efficiency (%) was determined by using Eq. (1) where A_1 is the total amount of carboplatin used in

nanoparticle preparation, and A_2 the amount of un-encapsulated carboplatin in the supernatant.

$$\text{Encapsulation Efficiency } (\%) = \frac{A_1 - A_2}{A_1} \times 100 \quad (1)$$

2.4. EGF conjugation to alginate-PAMAM hybrid nanoparticles

Conjugation of the EGF ligand to the surface of the hybrid nanoparticles was carried out by adding EDC (0.1 mmol), NHS (0.05 mmol) and EGF (1, 2 and 3 μg) to the CAPs (4 mg) dispersed in 1 mL PBS and mixed with a magnetic stirrer for 2 h in the dark.

The different EGF concentrations of 1, 2 and 3 μg/mL were tested to optimize the EGF concentration in reaction media with respect to the conjugation efficiency. After magnetic stirring, synthesized EGF-CAP nanoparticles were centrifuged at 8750*g* (9000 rpm) (Eppendorf MiniSpin® plus) and the pellet was washed two times *via* dispersion in deionized water and centrifuged again to remove the residues and unbound EGFs. Then the nanoparticles were frozen at −20 °C and lyophilized. The size distribution and morphology of EGF-CAPs redispersed in PBS buffer were determined with the DLS (Dynamic Light Scattering) by Zetasizer and SEM photographs taken by FEG-SEM, respectively. The amount of conjugated EGF per mass of nanoparticle was measured with the EGF ELISA kit. For the *in vitro* and *in vivo* experiments, APs, CAPs, EGF-APs, and EGF-CAPs were tested in terms of dispersibility/injectability in relevant media such as ultrapure water, PBS or cell medium. Especially, during the *in vivo* animal experiments, the dispersed samples in saline solutions were stored at 4 °C for 21 days. All samples were as easily dispersible and injectable by 22G needles.

2.5. In vitro cytotoxic effect and cellular uptake of nanoparticles

2.5.1. Cell culture

Human epithelial lung adenocarcinoma cells (A549 CCL-185) and human lung healthy bronchial epithelial cells (Beas-2b CRL-9609) were obtained from American Type Culture Collection (ATCC, Mannassas, VA, USA) and maintained in a Dulbecco's Modified Eagle Medium (DMEM): Ham's F12 Medium (1:1) supplemented with 10 % Fetal bovine serum, 1 % L-glutamine and 1 % Penicillin/Streptomycin (100×). Cells were cultured as a monolayer in a humidified incubator with 5 % CO_2 at 37 °C, using T-flasks with filter caps (Corning, USA) until reaching approximately 90 % confluence and splitted with 0.05 % trypsin-EDTA. All cell culture experiments were carried out as three independent replicates.

2.5.2. 2D cytotoxicity and cellular uptake

For cytotoxicity tests, in the first stage, A549 cells were seeded at at a concentration of 1×10^4 cells/well in a 96-well plate and incubated overnight. Thereafter, cell medium was removed and freshly prepared free carboplatin (72, 36, 18, 9, 4.5, 2.25 and 1.13 μg/mL) and nanoparticles carrying equivalent doses of the drug (2, 1, 0.5, 0.25, 0.125, 0.063 and 0.031 mg/mL) were added in wells in 100 μL culture medium. Also, empty nanoparticles were used at the same concentrations for comparative results and a growth medium as a control was added to each well. After dose-dependent 72 h of incubation, the culture medium was removed, 10 % MTT solution in serum-free medium (from 5 mg/mL stock solution) was added to each well and incubated at 37 °C for 3 h. Subsequently, MTT solution was removed and 100 μL DMSO was added to each well to solve formazan crystals. The absorbance at 570 nm was measured with a microplate reader (BioTek, Korea) and the percentage of cell viability and IC_{50} values were calculated by using GraphPad Prism 8.3.0 program. In the second stage, considering the calculated IC_{50} value of free carboplatin by dose-dependent assay, time-dependent incubations (24, 48 and 72 h) of EGF conjugated nanoparticles loaded with/without carboplatin and free carboplatin were investigated by MTT assay on both and A549 and Beas-2b cells [33,34].

For cellular uptake studies, A549 cells were seeded at a concentration of 1×10^5 cells/mL in a 24-well plate and incubated overnight. After the culture medium was removed, FITC-labelled nanoparticles carrying equivalent doses of carboplatin at IC_{50} concentration were added to the cells, the medium was refreshed after 6 h, and the cells were visualized under a fluorescent microscope (Zeiss Axio Vert.A1) after a total of 72 h.

2.5.3. 3D cytotoxicity and cellular uptake

For the 3D cytotoxicity test, the formation of 3D spheroid structures of A549 cells was first achieved using the 96-well ultra-low adhesion (ULA) plate technique. For this, A549 cells were seeded in 96-well ULA plates (Corning® CLS7007) at a concentration of 2×10^4 cells/well/150 μL, spun at 200 *g* for 2 min for better self-assembly, and cultured in DMEM-F12 medium for 96 h for formation of well-defined spheroids. After that, culture medium was removed carefully and dose-dependent free carboplatin (72, 36, 18, 9 and 4.5 μg/mL) and nanoparticles carrying equivalent doses of the drug (2, 1, 0.5, 0.25 and 0.125 mg/mL) were added to ULA plate wells in 150 μL culture medium. In parallel, empty nanoparticles were used at the same concentrations for comparative results and a growth medium as a control was added to each well. After 72 h incubation, MTT assay was performed and dissolved formazan crystals in DMSO from all wells was transferred to F-bottom 96-well plate without spheroids. Then, the absorbance was measured at 570 nm and the percentage of spheroid viability and IC_{50} values were calculated by using GraphPad Prism 8.3.0 program.

For 3D cellular uptake studies, after A549 cell spheroids were formed in 96-well ULA plates, FITC-labelled nanoparticles carrying equivalent doses of carboplatin at IC_{50} concentration were added to the wells in 150 μL culture medium. Then, the medium was refreshed after 6 h and spheroids were visualized under a fluorescent microscope (Zeiss Axio Vert.A1) after a total of 72 h.

2.6. Assessment of hemolysis

The assay was performed using the international ASTM standard practice F 756–00 [35] according to Dobrovolskaia et al. 2008 [36]. The fresh blood (4 mL) was collected from New Zealand rabbits (weighing 2000–2500 g) in Li heparinized tubes (Ethic approval date: 29.11.2023, no: 2019-079), centrifuged at 700*g* for 10 min and the pellet was washed three times with cold PBS (pH 7.4) and centrifuged again at 700*g* for 10 min. Subsequently, the pellet was resuspended in the same buffer at 20 % blood volume of total volume. The drug loaded and empty nanoparticles were tested in four concentrations (72, 36, 18 and 9 μg/mL) corresponding to the concentrations in cell culture studies. The samples were incubated for 60 min at 37 °C in a shaking water bath and then centrifuged at 700*g* for 10 min. Finally, the supernatant was measured at 540 nm by spectrophotometer to determine releasing hemoglobin amount. Triton X-100 at a stock concentration of 1 % (10 mg/mL) and PBS were used as positive and negative controls, respectively. The percent hemolysis (%) was determined by using Eq. (2);

$$\textit{Percent hemolysis}(\%) = \frac{\textit{absorbance of sample} - \textit{absorbance of negative control}}{\textit{absorbance of positive control} - \textit{absorbance of negative control}} \times 100 \quad (2)$$

According to the standard (ASTM F 756–00), percent hemolysis <5 % indicates that the test sample is not hemolytic, whereas >5 % hemolysis indicates a hemolytic state.

2.7. In vivo experimental model

2.7.1. Animals

The experiment was approved by the Ege University Local Ethical Committee for Animal Experiments (29.01.2020, no: 2019-079). All procedures were carried according to the Ethical guidelines for investigations of experimental pain in conscious animals [37]. BALB/c albino mice (6–7 weeks/20–25 g) were obtained from Ege University Laboratory Animal Application and Research Center and housed in steel cages at a temperature-controlled environment (22.0 ± 2.0 °C), where relative humidity was set at 45–65 % with 12 h light/dark cycles at Ege University ARGEFAR. Food and water were available *ad libitum*. During the study, the animals were fed with standard laboratory feed and water, *ad libitum*. Feed and water were changed daily and cage hygiene was carried out regularly. The animals were observed daily, and body weights were measured before and during the study.

2.7.2. Experimental design

A549 CCL-185 tumor cells (1×10^7 cells in 0.1 mL PBS) were injected subcutaneously into the right flank of BALB/c mice [38]. After 14 days of tumor implantation (tumor size reached approximately 50 mm^3 diameter), animals were randomly divided into 6 groups ($n = 6$) as listed below;

Control group: Mice were administered with 100 μL of saline (0.9 % NaCl) intraperitoneally i.p. once every 3 days for 3 weeks (n = 6).
Free carboplatin group: Mice were administered 20 mg/kg carboplatin in 100 μL of saline i.p. once every 3 days for 3 weeks ($n = 6$).
AP (Blank alginate-PAMAM nanoparticle) group: Mice were administered 20 mg/kg nanoparticles in 100 μL of saline i.p. once every 3 days for 3 weeks ($n = 6$).
CAP (Carboplatin-loaded alginate-PAMAM nanoparticle) group: Mice were administered 20 mg/kg carboplatin loaded nanoparticles in 100 μL of saline i.p. once every 3 days for 3 weeks ($n = 6$).
EGF-AP (EGF conjugated blank nanoparticle) group: Mice were administered 20 mg/kg EGF conjugated nanoparticles in 100 μL saline i.p. once every 3 days for 3 weeks (n = 6).
EGF-CAP (EGF conjugated carboplatin-loaded nanoparticle) goup: Mice were administered with 20 mg/kg EGF-conjugated nanoparticle-loaded carboplatin in 100 μL of saline i.p. once every 3 days for 3 weeks (n = 6).

2.7.3. In vivo imaging

To monitor the changes in tumor size during antitumor activity, 0.1 mL of 10 nmol/100 mL XenoLight RediJect 2-DG-750 Probe (Perkin Elmer Inc., MA) were injected intravenously to tail veins of animals at specified time intervals (0, 14 and 21 days). The images were taken under isoflurane anesthesia after 3 h of injection by the *In Vivo* Imaging System (IVIS Spectrum, Perkin Elmer Inc., MA) [39]. During the monitorization, the IVIS Spectrum device was set as Binning = 8, f/stop = 2, Excitation = 745 nm and Emission = 820 nm.

2.7.4. Biochemical analysis

At the end of 21 days, mice were sacrificed by taking blood from the heart under ketamine + xylazine overdose anesthesia. The biochemical analysis was performed with blood serum on Fujifilm FUJI DRI-CHEM NX500V IC device with Comprehensive S Panel kit including 13 parameters (Total protein-TP, Albumin-ALB, Globulin-GLOB, Glucose-GLU, Alanine aminotransferase-ALT, Gamma-glutamyl transferase-GGT, Alkaline phosphatase-ALP, Total bilirubin- TBIL, Total cholesterol-TCHOL, Creatinine-CRE, Blood urea nitrogen-BUN, Calcium-Ca, Inorganic phosphate-IP).

2.7.5. Histochemical and immunohistochemical examinations

Tissues (liver, kidney, and brain) and tumor sites were removed from each animal and collected in falcon tubes. After washing 2 times with PBS, the tissues were kept in 4 % paraformaldehyde for one night and subjected to a series of increasing degrees of alcohol and left to air dry. Dried samples were passed through xylol 3 times for 30 min until they became transparent. Paraffin-infused samples were kept in an oven at 58 °C for one night. The paraffin was renewed and waited for 2 h. This process was repeated two times respectively. Then, the tissues were embedded in paraffin and routine hematoxylin-eosin staining was performed on 5-micron sections taken from paraffin blocks. The images were taken and examined under the microscopy (BX5, Olympus, Tokyo, Japan) [40].

Detection of apoptosis in tumor tissue was demonstrated by the Promega cat G7360 with "DeadEnd™ Colorimetric Apoptosis Detection System (TUNEL) System". Sections were fixed in 4 % paraformaldehyde and incubated for 25 min at room temperature. Subsequently, samples were washed in PBS and permeabilized with 20 μg/mL Proteinase K solution per slide. Sections were then incubated with the reaction mixture containing biotinylated nucleotide and terminal deoxynucleotidyl transferase (rTdT) for 60 min at 37 °C. At the end of the period, the slides were washed with sodium chloride-sodium citrate buffer (SSC) and PBS buffer. Streptavidin HRP (horseradish peroxidase) was added to each slide and incubated for 30 min at room temperature. The slides were then stained with a diaminobenzidine (DAB) system and examined for the presence of apoptotic cells [41].

2.8. Statistical analysis

Statistical analysis of the experimental data was performed with SPSS version 25.0 (IBM Corp., Armonk, New York, USA). Data were expressed as the mean ± standard deviation (SD). One-way analysis of variance (ANOVA) followed by LSD test was performed for comparison between the groups *in vivo* experimental model. Additionally, one-way ANOVA Dunnett's multiple comparisons test and two-way ANOVA Tukey's multiple comparisons tests were performed for 2D—3D *in vitro* cytotoxicity assays. Values of $p \leq 0.05$ were regarded as statistically significant.

3. Results

3.1. Synthesis and characterization of alginate-PAMAM hybrid nanoparticles

Carboplatin loaded alginate-PAMAM hybrid nanoparticles (CAPs) were synthesized by microfluidic platform and then characterised. The effects of different PAMAM concentrations (0.04 and 0.08 mM), different flow rates (FRR 40, FRR 60 and FRR 80) and the presence of carboplatin drug on the size distributions of nanoparticles were examined (Fig. 1A). Increasing the PAMAM concentration from 0.04 to 0.08 mM led to a statistically significant ($p < 0.05$) increase in the mean size of the carboplatin-loaded CAPs nanoparticles (CAP4 and CAP8), but this trend was not valid for the empty counterparts (AP4 and AP8). In the microfluidic platform based on the flow-focusing principle, the FRR used exhibited a noticeable effect on the sizes of all the synthesized nanoparticle groups. As the flow rate of the PAMAM solution in the side channels was increased, the sizes of the synthesized CAP and AP nanoparticles decreased due to the increasing FRR. For example, when the FRR was increased from 40 to 60 and 80 in the empty nanoparticles (APs) synthesized with PAMAM at 0.04 mM concentration, nanoparticles with average sizes of 252.90 ± 12.86 nm, 191.50 ± 3.65 nm and 159.67 ± 6.63 nm were obtained, respectively. Similarly, carboplatin-loaded (CAPs) nanoparticles synthesized with PAMAM at 0.08 mM concentration were obtained with average sizes of 278.37 ± 8.41 nm, 230.37 ± 4.57 nm and 192.13 ± 4.15 nm with the same FRR, respectively. It is also important to note that the mean particle sizes of

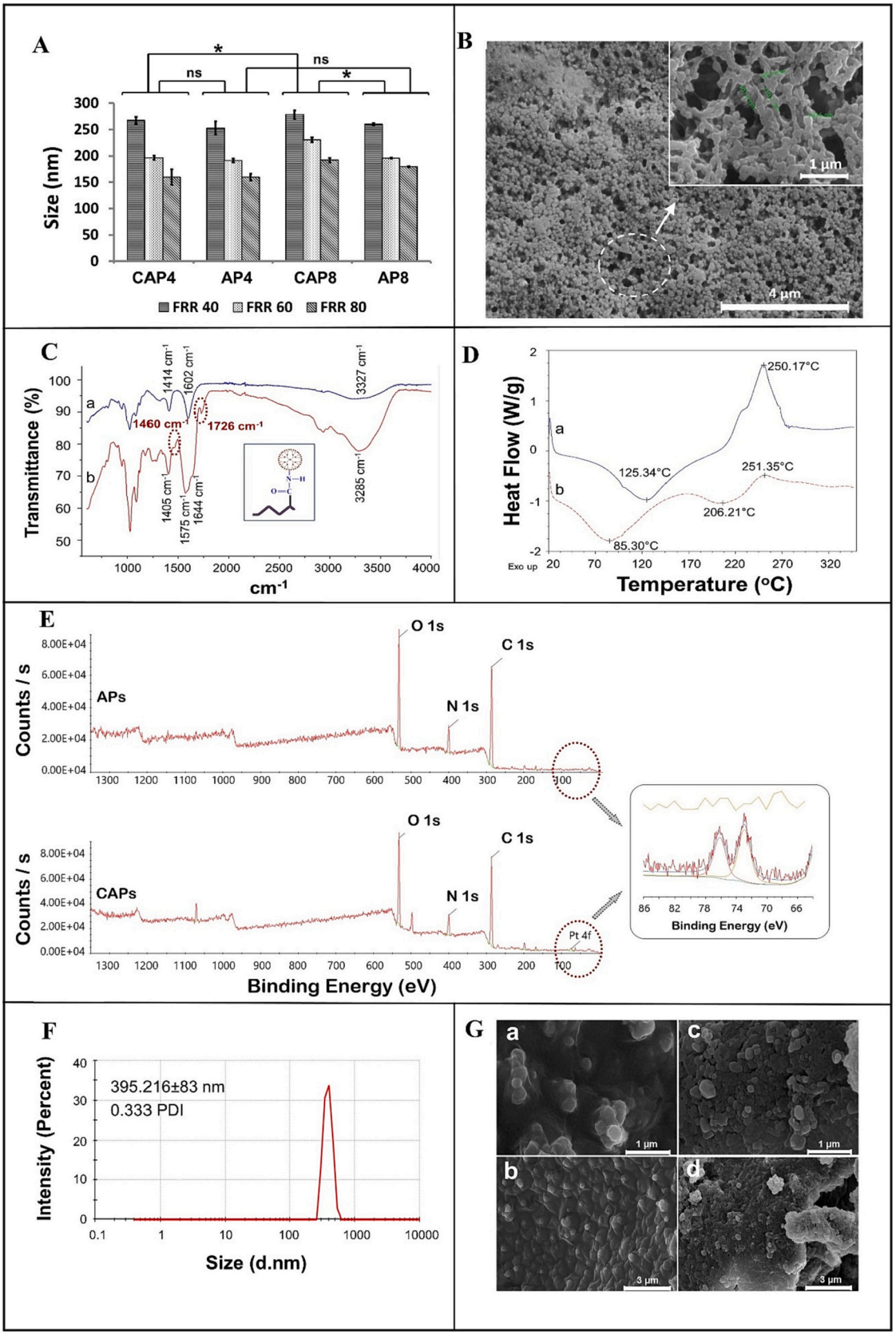

Fig. 1. Characterizations of synthesized CAPs and APs. Size distributions (*two-way ANOVA Tukey's multiple comparisons test, ns;$p > 0.05$, *;$p < 0.05$*) (A) and surface morphologies of CAPs (bar scales 1 and 4 µm, Thermo Scientific, Apreo S) (B). FTIR spectra (PerkinElmer Spectrum 100) (C) and thermal DSC characteristics (TA Instruments, Q20) (D) of alginate polymer (a) and APs (b). X-ray photoelectron spectra of CAPs compared to the APs (Thermo Scientific K-Alpha) (E). Size distrubutions of EGF-CAPs (Malvern Nano-ZS) (F) and SEM micrographs of EGF-APs (a; bar scale 1 µm and b; bar scale 3 µm) and EGF-CAPs (c; bar scale 1 µm and d; bar scale 3 µm) (Thermo Scientific, Apreo S) (G).

hybrid nanoparticles containing carboplatin were significantly ($p < 0.05$) higher when PAMAM was used at 0.08 mM concentration than their counterparts without carboplatin. On the other hand, the alginate-PAMAM hybrid nanoparticles synthesized under all conditions had very narrow distribution ranges (0.19–0.25 PDI values) and unimodal Gaussian curves. The smallest CAPs exhibited a mean size of 159.80 ± 14.79 nm with a PDI value of 0.192, which were synthesized with FRR 80 condition using a PAMAM concentration of 0.04 mM. The encapsulation efficiency of these CAPs was calculated as 40.45 ± 1.5 % and the corresponding drug loading content (DL) was 36 μg carboplatin per mg CAPs. The zeta potentials of CAPs were − 27.6 mV, −25.4 mV and − 23.8 mV with decreasing nanoparticle sizes, respectively, in conjunction with increased FRR conditions. When diluted with PBS, a zeta potential value of −55.7 mV was measured for the alginate due to negatively charged carboxyl groups (-COOH), whereas +36.7 mV for PAMAM dendrimer due to positively charged amine groups ($-NH_2$). Thus, alginate carboxyl groups probably predominated the surface of the synthesized hybrid nanoparticles, but dendrimer amine groups were partially present on the surface. Moreover, it was observed that not only the zeta potentials of nanoparticles but also their drug-carrying properties were affected due to increasing FRR conditions. Encapsulation efficiencies were 28.04 ± 1.6 %, 32.03 ± 0.33 % and 40.45 ± 1.5 % for FRR40, FRR60 and FRR80 conditions, respectively. Both carboplatin-loaded CAPs and empty APs exerted spherical and smooth surface morphologies (Fig. 1B).

In the FTIR spectrum of the alginate polymer used for synthesis, the peak at 3327 cm^{-1} corresponds to the −OH stretching vibration, while the bands at 1602 and 1414 cm^{-1} correspond to the asymmetric and symmetrical COO− stretching vibrations of the carboxylate salt groups, and the peak of 1110 cm^{-1} (C−O−C stretching) can be attributed to the saccharide structure of alginate (Fig. 1C). According to the FTIR spectra of the synthesized alginate-PAMAM hybrid nanoparticles, the band at 1405 cm^{-1} was probably from the carboxylate group of alginate residues, and the bands at 1644 cm^{-1} and 1575 cm^{-1} were from the amide I and II (-CO-NH-) of PAMAM residues [42]. Moreover, new bands appeared at 1460 cm^{-1} and 1726 cm^{-1}. Thermal characterizations of the synthesized hybrid nanoparticles were performed by DSC analysis (Fig. 1D), and the thermogram of the alginate used in the synthesis reaction showed an endothermic peak at 125 °C and an exothermic peak at 250 °C. On the other hand, in the thermogram of alginate-PAMAM hybrid nanoparticles, a two-peak endothermic region at 85.20 °C and 206.21 °C and an exothermic peak at 251.35 °C were observed. The XPS survey spectra of carboplatin-loaded or empty alginate-PAMAM nanoparticles (Fig. 1E) showed that both nanoparticles were mainly consisted of C, O, and N. Accordingly, photoelectron peaks of carbon (C 1 s) at ~286 eV, nitrogen (N 1 s) at ~401 eV, and oxygen (O 1 s) at ~532 eV were found. While empty samples did not have any Pt peaks, carboplatin-loaded nanoparticles had Pt peaks at ~73–76 eV only after etched 50 nm depth from the surface, which indicates that the carboplatin drug was embedded into the nanoparticle matrix rather than the adsorption to the surface.

3.2. Synthesis and characterization of EGF-conjugated alginate-PAMAM hybrid nanoparticles

After CAP nanoparticles were synthesized in the microfluidic platform, EGF has been conjugated to the surface of CAPs to synthesize EGFR-targeted EGF-CAPs. The mean sizes of EGF-conjugated nanoparticles increased to 395.216 ± 83 nm (PDI 0.333) after conjugation (Fig. 1F), possibly due to the use of magnetic stirrer rather than microfluidic conditions. However, when the surface morphologies of the EGF-conjugated nanoparticles were examined by SEM imaging (Fig. 1G), the spherical morphology was observed to be preserved after conjugation. EGF concentrations were tested as 1, 2 and 3 μg/mL in the conjugation reaction and the amount of EGF conjugated to the nanoparticles were determined as 0.108 μg, 0.386 μg and 0.462 μg per g of EGF-CAPs hybrid nanoparticles, respectively. The conjugated EGF on the surface gradually increased with respect to its concentration in the reaction media. Taking into account that the drug loading content was considered as 36 μg carboplatin/mg EGF-CAPs, 0.462 μg EGF/g EGF-CAPs were selected and used for *in vitro* cytotoxicity assays and *in vivo* animal experiments.

3.3. In vitro cytotoxicity and cellular uptake of nanoparticles in 2D/3D and hemolysis

In the framework of 2D *in vitro* cell culture assays, first of all, the cytotoxic effect of free carboplatin on A549 lung cancer cells was tested dose-dependently (72, 36, 18, 9, 4.5, 2.25 and 1.13 μg/mL) after 72 h exposure based on MTT cell viability assay, where the IC_{50} value was determined as 38.82 ± 6.7 μg/mL ($p < 0.0001$) (Fig. 2A**,a**). Next, the cytotoxic effects of nanoparticles that carry equivalent doses of carboplatin mentioned as CAP, EGF-CAP and carboplatin free EGF-AP, were also measured dose-dependently (2, 1, 0.5, 0.25, 0.125, 0.063 and 0.031 mg/mL) on 2D A549 cells.

Based on the results, carboplatin-free EGF-AP showed no cytotoxic effect on cells at all concentrations tested (above 70 % cell viability limit, $p > 0.05$), while the IC_{50} values were calculated as 30.07 ± 6.11 μg/mL for CAP ($p < 0.0001$) and 24.64 ± 2.96 μg/mL for EGF-CAP ($p < 0.0001$) nanoparticles (Fig. 2A,a). Then, the cytotoxic effect of CAP, EGF-AP and EGF-CAP nanoparticles carrying equivalent doses of carboplatin at IC_{50} value (38.82 ± 6.7 μg/mL) on both A549 lung cancer cells and Beas-2b healthy lung cells were tested time-dependently (24, 48 and 72 h) by using MTT assays. Carboplatin, CAP and EGF-CAP nanoparticles inhibited mostly A549 cancer cells in a time dependent manner, whereas no effective inhibition of carboplatin-free EGF-AP nanoparticles was observed for both A549 and Beas-2b cells (Fig. 2A,b). After 72 h, carboplatin and CAP reduced cell viabilities of A549 cells to 51.8 % and 50.8 %, and Beas-2b cells to 57.8 % and 56.9 % without any cell selectivity in a non-significant manner ($p > 0.05$). However, EGF-CAP nanoparticles inhibited the viability of A549 cancer cells to 37.4 % with a significant manner compared both to carboplatin inhibition at 72 h ($p < 0.05$) and to Beas-2b cells at 72 h ($p < 0.0001$) indicating a selective effect (Fig. 2A,b). Thereafter, A549 cellular uptake studies of FITC stained CAP and EGF-CAP nanoparticles were carried out to validate the superiority of EGF conjugation. The fluorescent microscope images at 72 h showed that, EGF conjugation increased the cellular uptake of EGF-CAP nanoparticles with an increased number of cells containing more FITC, thus indicating increased drug cytotoxicity by further inhibiting A549 cell viability (Fig. 2A,c). Additionally, the bright-field images of cellular uptake of FITC-labelled CAP and EGF-CAP nanoparticles (**Fig. S1**) show cell positions clearly.

Within the scope of 3D *in vitro* culture studies, the cytotoxic effect of dose-dependent free carboplatin, EGF-AP, CAP and EGF-CAP nanoparticles were tested in A549 cancer cell spheroids with MTT assay at 72 h exposure. The IC_{50} values were determined as 36.1 ± 19.6, 67.86 ± 19.24 and 35.89 ± 10.37 μg/mL for free-carboplatin ($p < 0.001$), CAP ($p < 0.01$) and EGF-CAP ($p < 0.001$), respectively, while carboplatin-free EGF-AP nanoparticles again showed no cytotoxic effect on spheroids at all concentrations tested (Fig. 2B,a). Moreover, an increase in cellular uptake of FITC+ cells was observed in A549 spheroids after EGF-CAP treatment compared to CAP, confirming the success of EGF conjugation strategy in a 3D setting (Fig. 2B,b). Apart from *in vitro* administration of the formulated nanoparticles, hemolysis test was carried out to observe the effects on erythrocytes (Fig. 2C). None of the concentrations of CAP and EGF-CAP have shown hemolysis on rabbit erythrocytes, while the two highest concentrations of EGF-AP (1 and 2 mg/mL) showed slightly hemolytic effects (5.6 % and 5.4 % respectively), as the results showing <5 % hemolysis are regarded as non-hemolytic and higher than 5 % hemolysis are regarded as haemolytic according to the international ASTM standard practice (F 756–00) [35].

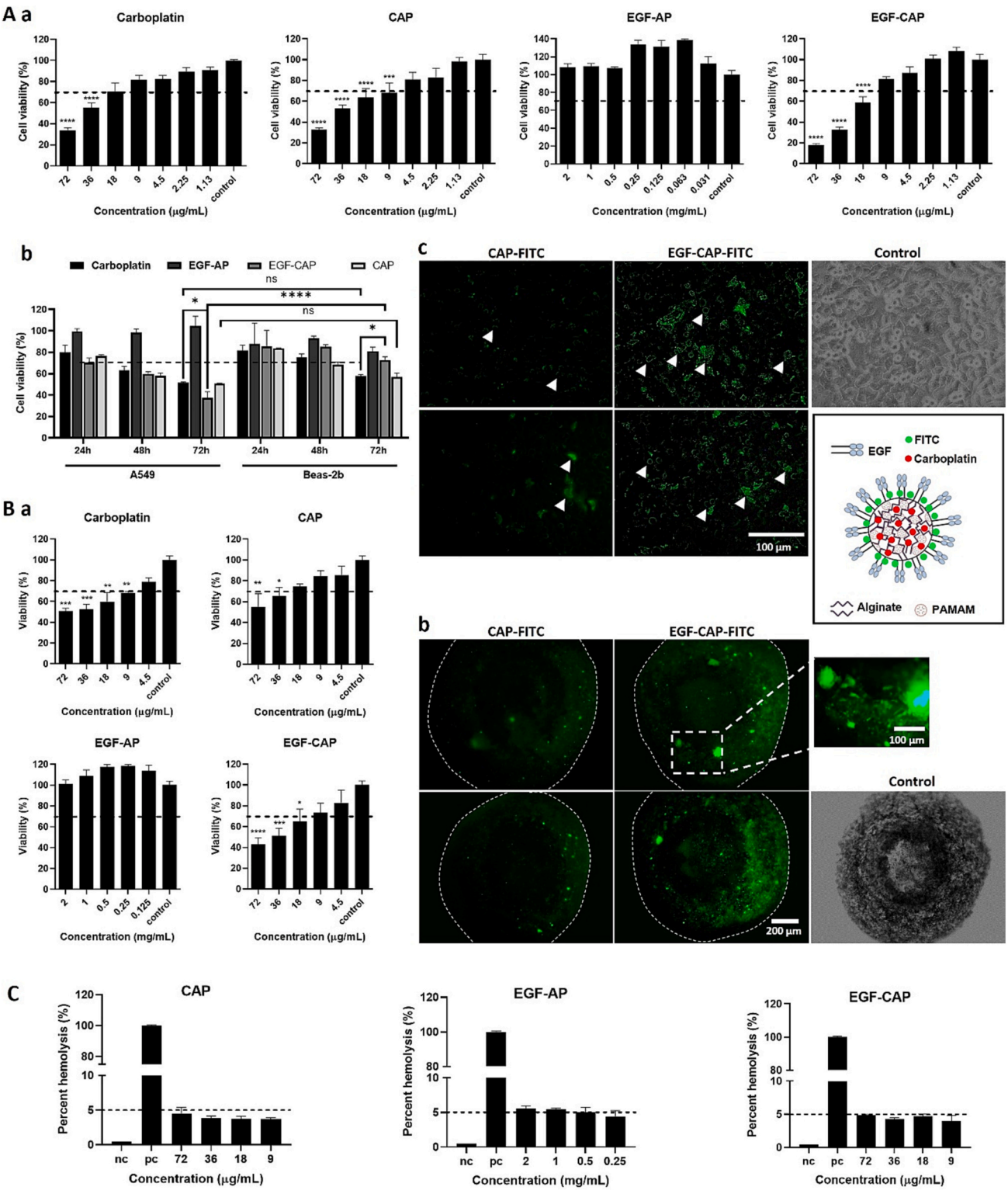

Fig. 2. Dose-dependent cytotoxic effects of free carboplatin and CAP, EGF-AP and EGF-CAP conjugated nanoparticles on A549 cells *(For all values below the 70 % viability limit, one-way ANOVA Dunnett's multiple comparisons test was performed versus each controls in all own groups, ***;$p < 0.001$, ****;$p < 0.0001$)* (a), time-dependent cytotoxic effects of free carboplatin CAP, EGF-AP and EGF-CAP conjugated nanoparticles on both A549 and Beas-2b cells (*two-way ANOVA Tukey's multiple comparisons test, ns;$p > 0.05$, *;$p < 0.05$, ****;$p < 0.0001$)* (b), the fluorescence microscopy images of the cellular uptake of FITC-labelled CAP and EGF-CAP nanoparticles by A549 cells (bar scale 100 μm, Zeiss Axio Vert.A1), white arrows show representative uptake cells) (c) for 2D monolayer culture (A). Cytotoxic effects of EGF-conjugated nanoparticles compared to the CAP and free carboplatin (*For all values below the 70 % viability limit, one-way ANOVA Dunnett's multiple comparisons test was performed versus each controls in all own groups, *;$p < 0.05$, **;$p < 0.01$, ***;$p < 0.001$, ****;$p < 0.0001$)* (a), and the fluorescence microscopy images of the cellular uptake of FITC-labelled CAP and EGF-CAP nanoparticles by A549 spheroids (bar scale 100 and 200 μm, Zeiss Axio Vert.A1) (b) for 3D culture (B). Percent hemolysis (%) ± SD of nanoparticles at different concentrations from three repetitive experiments (nc: PBS treated negative control; pc: Triton X-100 treated positive control, dashed lines shows 5 % hemolysis standart) (C).

Table 1
Total body weight values of animals in experimental groups starting from day 0 to 35, where tumor injection on day 14 is regarded as day 0 for the treatment.

Treatment groups	Total body weights (gram) (mean ± SD)					
	Day 0	Day 7	Day 14 (day 0)	Day 21 (day 7)	Day 28 (day 14)	Day 35 (day 21)
Control	26.4 ± 0.98	27.2 ± 1.41	26.6 ± 1.18	26.3 ± 1.21	26.0 ± 0.89	26.2 ± 1.58
Carboplatin	27.8 ± 1.31	27.3 ± 0.90	26.4 ± 0.97	26.4 ± 1.01	26.6 ± 1.00	27.1 ± 1.78
AP	27.9 ± 1.18	29.4 ± 2.12	27.1 ± 2.17	26.3 ± 1.26	28.3 ± 2.32	29.6 ± 2.98
CAP	28.7 ± 2.29	28.2 ± 1.92	27.3 ± 1.58	25.4 ± 2.20	26.4 ± 1.87	27.7 ± 1.35
EGF-AP	27.7 ± 1.30	27.3 ± 2.70	26.9 ± 2.14	27.1 ± 2.15	26.8 ± 1.98	27.5 ± 1.74
EGF-CAP	28.6 ± 2.32	28.5 ± 2.01	27.7 ± 2.10	26.3 ± 1.99	26.8 ± 1.56	26.7 ± 1.45
F	0.856	1.977	0.895	1.230	1.023	0.482
P	0.095	0.143	0.545	0.354	0.166	0.826

3.4. *In vivo experimental model*

3.4.1. *Total body weights*

During the study, weight losses not exceeding 20 % of the initial weights were noted (Table 1), whereas no deaths were observed in the experimental groups. The tumor injection on day 14 was accepted as day 0 for the treatment, and no statistically significant differences were noted with respect to the body weights in any of the treatment groups when compared to the control.

3.4.2. *In vivo imaging*

The IVIS images of animals were captured on day 0, 14 and 21 (Fig. 3**)** and the region of interest (ROI) values were presented to evaluate the cancerous regions (Table 2). The decreases and increases in cancerous areas of animals in groups were compared by proportioning total ROI values of days 0 and 21. When the comparative images taken with the IVIS imaging system on day 0 and 21 are examined, tumor tissue volumes were observed to increase by 117 % in the free carboplatin and 234 % in blank AP groups but not as much as saline control group (285 %). On the other hand, CAP decreased tumor volume by 61 % from day 0 to 21, and tumor tissues of mice completely disappeared in the EGF-CAP group at the end of 21 day treatment. It is worth to mention that renal metastases supporting lung metastasis were observed in control animals in *ex-vivo* studies (**Fig. S2**).

3.4.3. *Biochemical analysis*

Various parameters were evaluated as part of the biochemical analysis of the blood taken from the mice in the experimental groups at the end of the treatments (Table 3). Considering the control group and the reference values of the specified breeds [43], it was observed that indicators (TP, ALB) of general physical conditions were both within reference values for animals in all experimental groups and the general health status of the animals were found to be good.

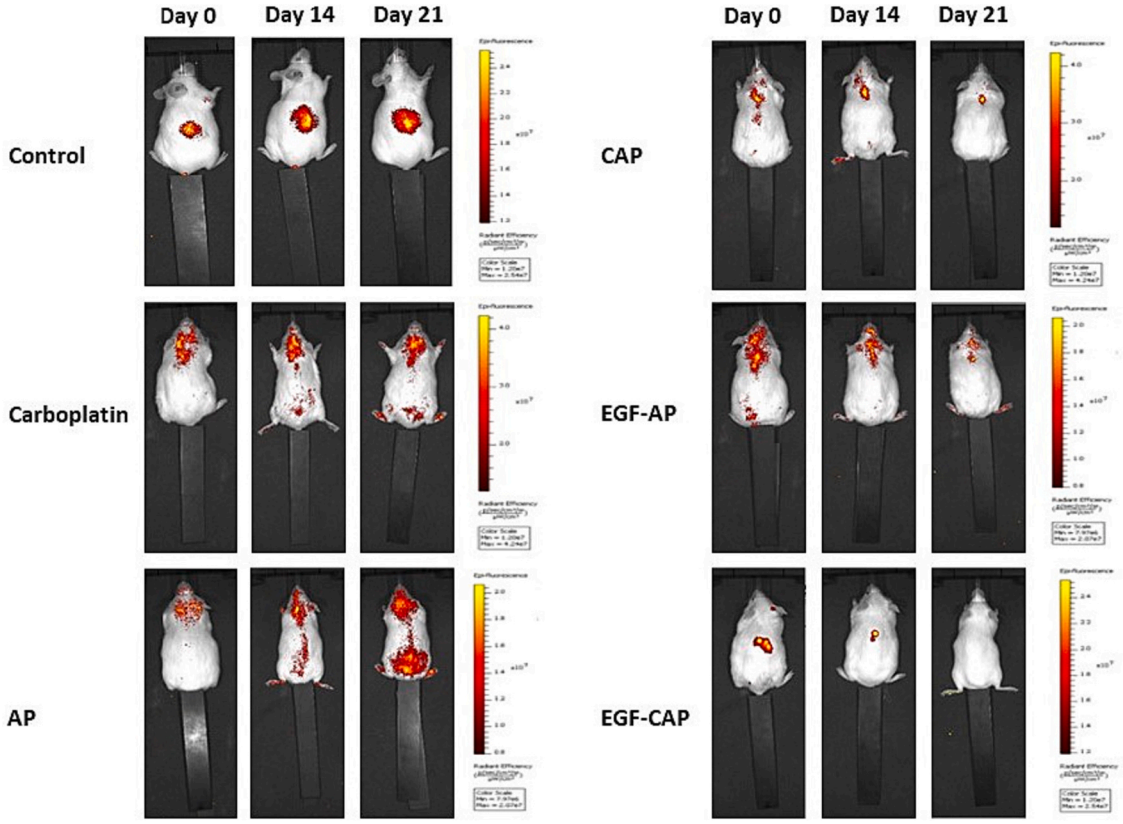

Fig. 3. *In vivo* imaging of tumors in experimental animal groups at day 0, 14 and 21. After 3 h of injection, the images were captured on the IVIS Spectrum with binning = 8, f/stop = 2, excitation = 745 nm and emission = 820 nm.

Table 2
The region of interest (ROI) values of animals in experimental groups.

Treatment Groups	(Total ROI values ±SD) × 10^8			ROI value changes (%) from day 0 to day 21
	Day 0	Day 14	Day 21	
Control	1.540 ± 0.109	4.073 ± 0.030	5.937 ± 0.224	285
Carboplatin	1.583 ± 0.096	3.348 ± 0.135	3.440 ± 0.092	117
AP	1.692 ± 0.201	4.103 ± 0.213	5.667 ± 0.242	234
CAP	1.468 ± 0.098	1.271 ± 0.117	0.573 ± 0.098	−61
EGF-AP	1.939 ± 0.168	2.235 ± 0.075	2.273 ± 0.134	17
EGF-CAP	1.421 ± 0.082	1.212 ± 0.120	–	−100

Table 3
Biochemical analysis values of animals after the nanoparticle treatments.

Biochemical parameters	Treatment groups					
	Control	Carboplatin	AP	CAP	EGF-AP	EGF-CAP
Total Protein (g/dL)	4.8 ± 0.31	5.2 ± 0.16	5.0 ± 0.47	4.8 ± 0.33	4.8 ± 0.54	4.9 ± 0.15
ALB (g/dL)	2.6 ± 0.14	3.1 ± 0.40	2.4 ± 0.28	2.4 ± 0.12	2.6 ± 0.16	2.2 ± 0.22
GLOB (g/dL)	2.2 ± 0.17	2.1 ± 0.18	2.6 ± 0.25	2.4 ± 0.16	2.2 ± 0.19	2.7 ± 0.20
GLU (mg/dL)	178 ± 10.0	190 ± 15.9	182 ± 11.3	174 ± 13.7	210 ± 18.4	156 ± 8.9
ALT (U/L)	55 ± 3.96	41 ± 7.76	32 ± 6.41	142 ± 12.8	37 ± 5.62	39 ± 8.55
GGT (U/L)	< 10	35 ± 5.72	< 10	< 10	< 10	< 10
ALP (U/L)	< 14	< 14	< 14	< 14	< 14	< 14
TBIL (mg/dL)	1.1 ± 0.31	3.1 ± 0.34	1.0 ± 0.15	1.1 ± 0.14	1.9 ± 0.40	0.7 ± 0.23
TCHOL (mg/dL)	90 ± 6.89	72 ± 4.78	86 ± 5.81	88 ± 5. 49	53 ± 3.17	69 ± 7.00
CRE (mg/dL)	0.20 ± 0.02	0.40 ± 0.03	0.26 ± 0.01	0.27 ± 0.03	0.29 ± 0.02	0.42 ± 0.04
BUN (mg/dL)	17.5 ± 1.29	21.1 ± 1.54	16.8 ± 1.58	24.7 ± 1.11	22.6 ± 0.95	19.8 ± 1.44
Ca (mg/dL)	8.9 ± 1.03	< 4.0	< 4.0	< 4.0	< 4.0	< 4.0
IP (mg/dL)	7.7 ± 0.16	5.6 ± 0.81	6.3 ± 0.34	5.2 ± 0.28	6.7 ± 0.33	6.1 ± 0.19

3.4.4. Histological findings

When the liver tissues were evaluated in terms of general histological parameters, diffuse vascular congestion and edema were observed in the vena centralis, vena porta interlobularis, and sinusoids in the control group (Fig. 4A). Vacuolar degeneration and hepatocytes with pycnotic nuclei were prominent in the periphery of the hepatic lobule. Also, Kupffer cell activation was noteworthy. In the carboplatin treated group, leukocyte infiltration with diffuse vascular congestion and edema was observed in the vena centralis, vena porta interlobularis and sinusoids. Necrotic hepatocytes were densely seen in the remark cords surrounding the vessels. In addition to focal leukocyte infiltration, an increase in Kupffer cell activation was observed clearly (Fig. 4B). Vascular congestion and edema were noted in the vena centralis, vena porta interlobularis and sinusoids in the AP group, less than the carboplatin group, however at the same level as the control group. In the periphery of the hepatic lobule, hepatocytes with eosinophilic cytoplasm were prominent. In addition to focal leukocyte infiltration, an increase in Kupffer cell activation is noteworthy (Fig. 4C). In the hepatic lobule in the CAP group, hepatocytes arranged as cords (Remark cords) spreading from the vena centralis to the periphery of each lobule, sinusoids, Kupffer cells covering the sinusoids, and round or polyhedral shaped hepatocytes exhibited normal appearances. As such, stromal areas exhibited normal appearances (Fig. 4D). The EGF-AP group had similar histological features with that of CAP group (Fig. 4E). The liver tissue of the EGF-CAP group was also observed to have histological features like CAP and EGF-AP groups (Fig. 4F).

With respect to lung tissues, stromal and parenchymal areas were evaluated as normal in the control group. Histological appearances of terminal bronchioles, respiratory bronchioles, ductus alveolaris and alveoli pulmonalis were also normal. Focal histological changes were observed in the stromal and parenchymal areas in the carboplatin group. Inflammation was observed in terminal bronchiole lamina propria and multiple alveoli. In addition, intraalveolar hemorrhages were noteworthy. In addition, intraalveolar edema with alveolar wall congestion and alveolar wall thickening were noted in some alveoli. Lung tissues of the AP group showed similar histological findings with that of the carboplatin group, with signs of minor inflammation in the alveoli and intraalveolar hemorrhage. On the other hand, inflammation was detected in the terminal bronchiole lamina propria of the lung tissue of the CAP group and in many alveoli. In addition to intraalveolar hemorrhages, very intense intraalveolar edema with alveolar wall congestion and alveolar wall thickening were evident in multiple alveoli. When this group was compared with carboplatin and AP groups, these findings were considered quite severe. The lung tissues of EGF-AP group were found to have histological features close to the control group. Also in this group, intraalveolar hemorrhage and edema were seen in small number of alveoli. Stromal and parenchymal areas in the lung tissue of the EGF-CAP group were observed to be in normal appearance. The histological appearances of terminal bronchiole, respiratory bronchiole, ductus alveolaris and alveoli pulmonalis were normal.

In all experimental groups, the stromal and parenchymal areas of the kidney tissue cortex and medullary layers were evaluated in terms of histological parameters, and the stromal areas in the cortex and medullar regions were observed to have normal appearances. As such, Bowman's capsule, Bowman's space and glomeruli forming the renal corpuscle exhibited normal appearances in the parenchymal areas of the cortex layer. Proximal and distal tubules and tubules epithelial cells appeared normal as well. The tubules and tubule epithelial cells in the medullary areas were also evaluated to have normal histological structures (Fig. 4, *right column*). In all experimental groups, tumor tissue shrinkage was detected in the EGF-AP and EGF-CAP treatments when compared to the control group (Fig. 5A-F, *top panel*). These findings were in consistent with the IVIS images. However, the highest TUNEL immunoreactivity was detected in the EGF-CAP group (Fig. 5A-F, *bottom panel*).

4. Discussion

Carboplatin and cisplatin, which are platinum-based drugs, have been used in the treatment of many malignancies. As a second-generation antineoplastic drug, carboplatin is widely recommended especially for chemotherapy in lung, colon, breast, cervix, testicular and digestive system cancers [44]. Even though the overall drug efficacy between the two agents is similar, differences in drug-related toxicity

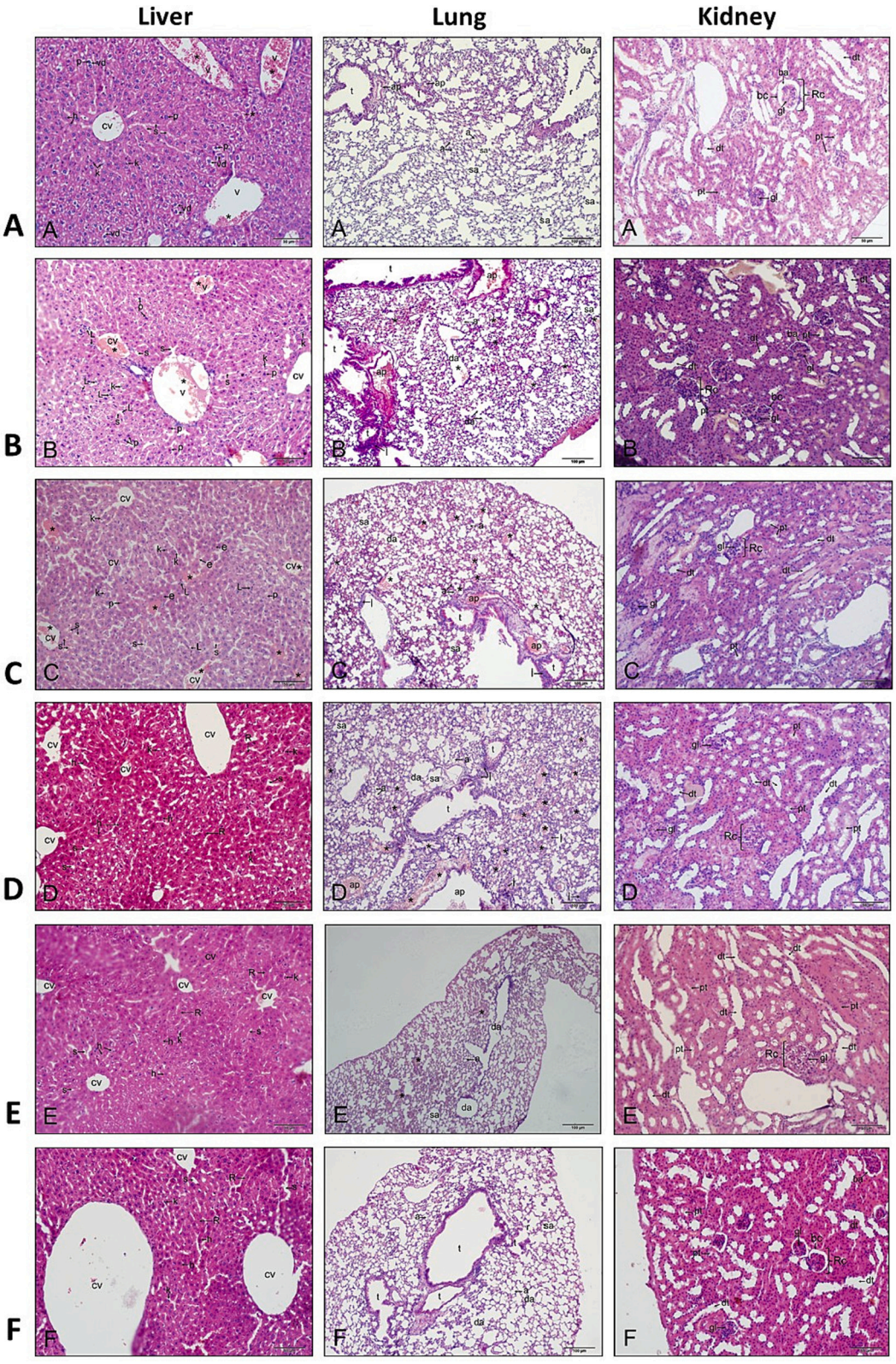

Fig. 4. Histological examination of liver, lung, and kidney tissues at all experimental groups (A: Control group; B: Carboplatin group; C: AP group; D: CAP group; E: EGF-AP group; F: EGF-CAP group). R, Remark cords; h, hepatocyte; cv, vena centralis; v, vena porta interlobularis; k, Kupffer cell; s, sinusoid; et al., vacuolar degeneration; p, pycnotic nucleus; e, eosinophilic cytoplasm; *, congestion and edema; L, leukocyte infiltration. Rc, Renal corpuscle; bc, Bowman's capsule; ba, Bowman interval; gl, glomeruli; pt., proximal tubule; dt, distal tubule. t, terminal bronchiole; r, respiratory bronchiole; ap, arteria pulmonalis branch; da, ductus alveolaris; sa, saccus alveolaris; a, alveoli pulmonalis; *, hemorrhage and edema; i, inflammation. Magnification, X20; dye, Hematoxylin- Eosin.

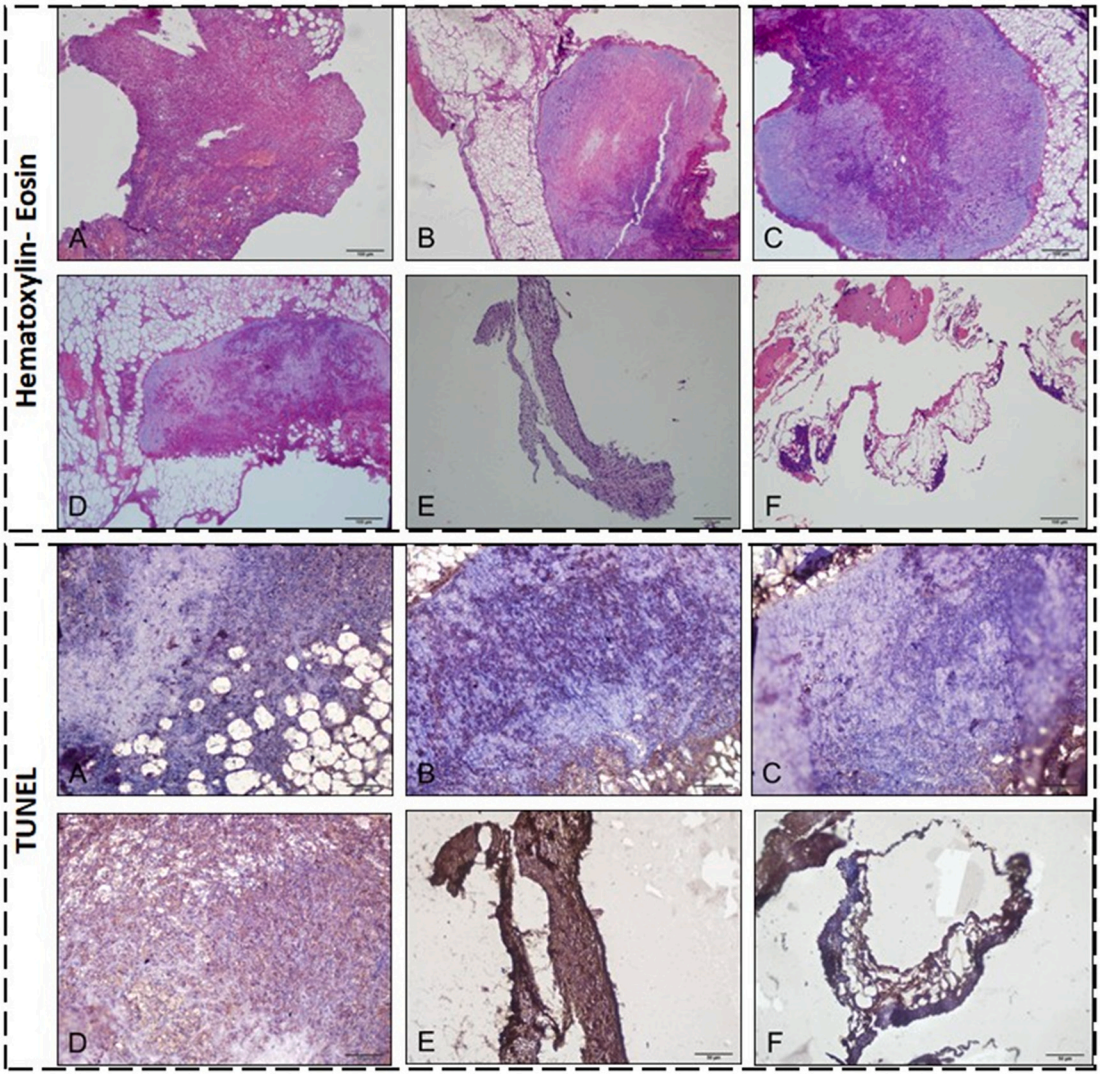

Fig. 5. Histological examination of tumor tissue at all experimental groups (A: Control group; B: Carboplatin group; C: AP group; D: CAP group; E: EGF-AP group; F: EGF-CAP group). Magnification, X10. Hematoxylin- Eosin (Two top panels). TUNEL immunohistochemistry stainings depicting the tumor tissue shrinks in the EGF-AP and EGF-CAP groups and the highest TUNEL immunoreactivity in the EGF-CAP group (Two bottom panels).

profiles are apparent. Cisplatin is associated with emesis, nephrotoxicity, and neurotoxicity, whereas the myelosuppressive effects of carboplatin lead to hematologic toxicities [45]. As such, multiple doses might be administered in multiple cycles (over six cycles) to achieve necessary tumor inhibition. Therefore, various attempts have been devoted to increase the effectiveness of platinum compounds and thereby reduce the number of required dosing cycles [44]. For example, conjugation of PAMAM with cisplatin resulted in relatively higher drug loading content [46]. However, there are limited studies with respect to carboplatin formulated drug delivery systems. In one of these studies, carboplatin-loaded nanoparticles were synthesized using poly(D-lactide-*co*-glycolide) (PLGA) [44] and polymethylmethacrylate (PMMA) [47], but drug loading contents were very low, thereby the efficient carboplatin loading and targeting with nanoparticles still remains as a major challenge. The targeting of a developed drug delivery system to a specific tissue or cell can be performed actively or passively. Active targeting is a strategy that occurs by binding specific ligands for receptors that are overexpressed in cancer tissues to the surfaces of drug carrier nanoparticles. The ability to increase the accumulation, adhesion, and cellular uptake of the nanoparticles and thus the drug in specific tissues is the basis of this receptor-targeted ligand-binding strategy. EGFR as a receptor tyrosine kinase is frequently overexpressed in non-small cell lung cancer (NSCLC), which constitutes the majority (about 75 %) of lung cancers, and NSCLCs are still difficult to treat due to pathological mechanisms that are not well understood. Current research on EGFR-targeted nanoparticles includes antibodies and antibody fragments, such as cetuximab and trastuzumab, which are FDA-approved antibody immunotherapies [48,49]. In parallel with antibody-mediated EGFR targeting, there has been increasing interest in using the natural ligand of EGFR, EGF. Such a small size compared to the antibodies has made EGF an attractive targeting ligand for nanoparticular systems. Additionally, unlike the natural ligand EGF, the use of antibodies for targeting can trigger severe immune responses that lead to cytotoxicity [12]. In this study, EGF conjugation to the surface of carboplatin loaded alginate-PAMAM hybrid nanoparticles was performed with the EGF ligand for active targeting, which increases the accumulation, adhesion and cellular uptake of the synthesized nanoparticles, thus carboplatin drug specifically in tumor tissues instead of healthy tissues. Due to its protein structure, EGF contains both carboxylic acids and primary amines (C- and N-termini, as well as amino acids found in the side chains of EGFs). Therefore, the aim was to form an amide bond between the alginate carboxylic groups on the surface of hybrid nanoparticles and the amine groups of EGF using carbodiimide chemistry using EDC and NHS. Achieving monodispersity is another milestone during

nanoparticle synthesis. Compared to the traditional preparation techniques, microfluidic platforms enable the production of nanoparticles with narrow size distributions [50]. For the synthesis of carboplatin-loaded alginate-PAMAM hybrid nanoparticles in the flow-focusing microfluidic platform, increase in the PAMAM concentration has led to a statistically significant ($p < 0.05$) increase in the mean size of CAP nanoparticles (CAP4 and CAP8). In consistent with this result, the lowest size of anthocyanin loaded silica/PAMAM hybrid nanoparticles have been obtained using the lowest concentration (5000-fold dilution) of PAMAM dendrimer (G4) as an inorganic precursor in our previous study [51]. In the microfluidic platform based on the flow-focusing principle, the mean sizes of the synthesized CAP and AP nanoparticles decreased as the FRR increased from 40 to 80. This might be associated to the shorter residence times at relatively high FRRs for the growth of the nanoparticle matrix, which occur due to the chemical bonding and electrostatic interactions between the lateral PAMAM dendrimer flows and the central alginate flow in the flow-focusing region [52–54]. The negative charges of alginate-PAMAM hybrid nanoparticles (−23.8 to −27.6 mV) were less than alginate polymer (−55.7 mV) alone, probably positively charged amine groups of the dendrimer have reduced the domination of the negative charge of alginate carboxyl groups on the surface of the synthesized hybrid nanoparticles. The highly negative surface charge can enhance particle stability by avoiding particle aggregation and fusion through electrostatic repulsion forces [50,55]. As mentioned earlier, the high FRR condition provides a much shorter time for the alginate and PAMAM components to bind for particle nucleation and growth, as well as for the diffusion of carboplatin molecules from the central polymer phase to the aqueous PAMAM phase coming from the side channels. Thus, possibly encapsulation of larger amounts of drug could be achieved. The hypothesis that nanoparticles can encapsulate more drugs with decreasing size is also compatible with a similar study in the literature in which chitosan nanoparticles loaded with thymoquinone and L-ascorbic acid were developed [56]. Moreover, the carboplatin loading content of EGF-CAPs (36 μg/mg) was quite higher than in previous studies using PLGA (drug loading content of 3.46 μg/mg) [44] and PMMA (drug loading content of 8.6 μg/mg) [47]. To hybridize the alginate polymer chain with the PAMAM dendrimer, the alginate carboxyl groups (-COOH) must be activated and then covalently attached to the -NH_2 amino groups on the PAMAM dendrimer surface by carbodiimide chemistry. The new band appearing at 1460 cm^{-1} in the FTIR spectrum of alginate-PAMAM hybrid nanoparticles showed the formation of an amide II (bandδ N—H bending) bond formed by carbodiimide chemistry between the alginate-COOH and dendrimer-NH_2 groups, while the new band appearing at 1726 cm^{-1} was derived from the carbonyl group (C = O). Thermal characterization of alginate-PAMAM hybrid nanoparticles by DSC analysis revealed a two-peak endotherm region, which is considerably wider than polymeric alginate, thought to be associated with high water loss due to both moisture residues in the nanoparticles and dehydration of the alginate saccharide structure. The exothermic and endothermic peaks of the alginate polymer used in the synthesis reaction were in agreement with the literature [57]. In both hybrid nanoparticles and alginate in polymer form, very similar exothermic regions have occurred at about 250 °C corresponding to depolymerisation and decarboxylation of the polymer chain. XPS analysis showed that the carboplatin drug was embedded into the alginate-PAMAM hybrid nanoparticle matrix because 50 nm etching depth was used in our study, even if elemental composition analysis of XPS is performed at 10 nm from the top surface generally [58]. The encapsulated drug location in the nanoparticle matrix or its crystalline/amorphous structure in nanoformulations could affect the release profile of the drug depending on the release media. Our previous study on resveratrol-loaded silica-PAMAM inorganic hybrid nanoparticles showed that the local arrangement of resveratrol in crystalline form in the silica-PAMAM matrix led to a slower release at both pH values of 1.2 and 7.4, where the cumulative releases were <25 % within 2 h [59]. Moreover, the release of encapsulated biomolecules from a nanoparticle matrix is generally governed by matrix erosion or diffusion [50]. Thus, the degradation rate of the nanoparticle matrix or diffusion coefficient of biomolecule across the matrix plays a major role in the release rate.

After the conjugation of EGF ligand to the surface of CAPs, EGF-CAP hybrid nanoparticles still exhibited spherical morphologies with mean sizes of 395.216 ± 83 nm (PDI 0.333). Although the mean size of EGF-CAPs increased after conjugation, still remained smaller than 400 nm, thus retaining their extravasation potentials into tumor tissues with the EPR effect [60]. The content of conjugated EGF on the surface of EGF-CAP hybrid nanoparticles was evaluated using the EGF ELISA-kit, as in another study [19], our results showed that the conjugated EGF on the surface gradually increased with respect to its concentration in the reaction media. It was calculated that a maximum of 0.462 μg EGF was conjugated on the surface of EGF-CAPs per gram of nanoparticles. The quantity of covalently linked EGF on the amine-functionalized hollow mesoporous silica nanoparticles has also been found to gradually increased with respect to increasing concentration of EGF in the reaction media [14]. This result indicates that the amount of EGF-ligand could be controlled in the conjugation stages by changing the EGF concentration.

The cells are more robust and aggregated into a clump in 3D spheroid culture compared to 2D monolayer culture, and the interaction of the cells remaining in the inner parts with the drug is restricted. Thus, both the evident cellular uptake ratio and cytotoxic effects of drugs are slightly less visible in 3D [61–63]. With targeted nanoparticular delivery systems, better drug uptake into 3D spheroids can be achieved. The size, surface charge, morphological condition, deformability, conjugated-ligands and other chemical/physical properties of the nanoparticles affect these mechanisms [64]. As such, inducing receptor-mediated endocytosis by ligand binding to the surface of nanoparticles is a viable strategy to facilitate tumor cell-specific internalization [65]. Tumor cells are known to overexpress various receptors on their surface, where binding of ligands to these receptors is involved in multiple signalling cascades that aid tumor growth and proliferation, angiogenesis, survival at different oxygen levels and pH conditions, apoptosis resistance, and metastasis [66]. EGFR, a receptor tyrosine kinase, is frequently overexpressed in NSCLC. EGF, the natural ligand of EGFR, is a 6-kDa protein made of 53 amino acid residues. Its small size, three disulfide bonds and tryptophan-tyrosine residues make it an attractive targeting ligand for nanoparticular systems [12,15,67]. As a result of the functionalization of the surfaces of carboplatin-loaded EGF-CAP hybrid nanoparticles with EGF as a ligand, higher cytotoxicity values were achieved in both 2D and 3D tumor cells, compared to free carboplatin and unconjugated nanoparticles. Nonetheless, carboplatin-loaded EGF-CAP hybrid nanoparticles even at the highest concentration have not exerted any hemolytic effect.

Modeling human tumors in animals for cancer research is a widely used approach [68,69]. Cancer treatments including surgery, radiation, chemotherapy and all related procedures can damage the healthy tissues as well as the cancerous tissues. Animal models coupled with nano-based treatments can enable targeting to specific cancer tissue by accumulating at the tumor location with different administration routes of drugs [70]. The use of imaging systems allow the monitoring of cancer cells in living animals for prolonged periods depending on the treatment duration. To verify the results we obtained in 3D *in vitro* cell culture, *in vivo* antitumor activities of carboplatin, AP, CAP, EGF-AP and EGF-CAP were evaluated in an A549 cell line induced xenograft tumor animal model and followed up with *in vivo* imaging, which is indispensable, allowing high tissue penetration up to a few centimeters deep. Quantitative analysis of tumor tissue showed that the fluorescence intensity determined by the *in vivo* imaging in tumor tissue treated with EGF-CAP was much lower, indicating a smaller tumor size than in other groups. *In vivo* targeting ability of EGF-conjugated-CAPs is in agreement with the study of Tseng et al. (2007), where an additional amount of EGF-bonded-gelatin nanoparticles was reported to accumulate in the cancerous lung of CB-17/lcrCrl-scid-bg mice *via* EGFR targeting [16]. According to the IVIS imaging, while free carboplatin could not exert

any antitumorigenic effect on the A549 cell line-induced xenograft tumor animal model, CAPs probably extravasated into tumor tissues with the EPR effect and exerted anti-tumor effect. Interestingly, a similar trend was also observed in EGF-conjugated AP blank nanoparticles, where tumor volume was decreased by 67 %, whereas 322 % increase was noted for AP nanoparticles. Thus the decrease is not associated with the presence of alginate-PAMAM but rather internalization of EGF-APs due to the binding of EGF ligand to EGFR receptor on the surface of tumor cells [12]. As expected, the tumor tissue of mice completely disappeared in the EGF-CAP administrated group at the end of day 21. In a previous report, the growth inhibitory rate of EGF-conjugated paclitaxel-loaded polymeric lipid-based nanoparticles was significantly higher than their non-EGF-bearing counterparts [17]. When high-density lipoprotein (HDL)-mimicking peptide-lipid nanocarriers were directed to EGFR with EGF ligand conjugation, it was observed that a coordinated dual receptor (EGFR and SR-BI) targeting phenomenon led to enhanced cargo delivery [71]. Furthermore, EGFR-overexpressing MDA-MB-468 tumors in athymic Nu/Nu mice treated with the recombinant murine EGF conjugated 4-(N)-stearoyl gemcitabine nanoparticles grew significantly slower than in mice treated with untargeted nanoparticles [18].

Determination of biochemical parameters provides vital information not only about the clinical status of the animals but also the metabolic functions of tissues and organs. The metabolic state of all tissues is completely different. As such, different physiochemical and pharmacokinetic profile of drugs effect the fate in the body. On the other hand, particle size is a key factor on efficacy, uptake by organs, prolonged blood circulation time and bioavailability in the body [72]. Variations in the biochemical parameters of rodents may be related to species, strain, and genotype, which might be influenced by other factors such as age, diet and environment [73]. Therefore, we included 6–7 weeks of BALB/c mice weighing about 20–25 g to eliminate some of the variations. Although reference values cannot be specified for many parameters, we evaluated biochemical parameters of the experimental groups considering the control group and reference values of the specified breeds [43]. Total protein (TP) is an important determinant of metabolic homeostasis due to proteins found in all components of cells. Indeed, TP forms the basis of both the structure and the function, which is commonly evaluated in conjunction with ALB and GLOB [74]. In the present study, TP and ALB values, which are indicators of general physical condition, were both within reference values for animals in all experimental groups and the general health status of the animals were found to be good. However, as indicators of the hepatic system GGT and TBIL were significantly high in the free carboplatin group. The states of oxidative stress like carcinogenesis was reported to increase glutathione and GGT levels [75], and inhibition of GGT activity completely blocks the nephrotoxicity of another platinum-containing drug, cisplatin [76]. Thus, the changes in liver histology in free carboplatin group suggests that the increase of GGT and TBIL levels are related to carboplatin administration. Additionally, ALT level was significantly high in the CAP group (142 ± 12.8 U/L) compared to the control (55 ± 3.96 U/L), which generally indicates hepatic lesions and damaged hepatocytes [73]. Nevertheless, the other hepatic system indicators, GGT and TBIL were at normal ranges, and liver histology displayed a normal appearance in the CAP group. Considering EGF-CAP group, both ALT and GGT levels decreased to 39 ± 8.55 U/L and < 10 U/L, respectively and a 4.4-fold decrease was noted in TBIL value compared to the CAP group. Since EGFR is known to be an important regulator of hepatocyte regeneration [77,78], the conjugation of EGF to the surface of CAPs might have induced ligand-mediated receptor endocytosis in the nontumor-bearing liver, possibly resulting in the recovery of hepatic system indicators. This idea has been supported by the liver histology with the normal appearance in the EGF-CAP group. Renal function evaluation was based on measurement of CRE and BUN. Indeed, BUN produced in the liver is the major nitrogen metabolite derived from protein breakdown, where 90 % are excreted by the kidneys [73]. We also quantified BUN levels in all treatment groups as nephrotoxicity is commonly associated with platinum-based drugs [79]. In our study, when renal system indicators (BUN, CRE, IP), vascular system (TCHOL) and bone system indicators (Ca, IP) were evaluated, the application groups showed values compatible with the control group and the reference values. In this study, the biochemical analysis was performed with Comprehensive S Panel kit including 13 parameters (TP, ALB, GLOB, GLU, ALT, GGT, ALP, TBIL, TCHOL, CRE, BUN, Ca, IP). However, new biosensor designs based on localized surface plasmon resonance (LSPR) technology for the detection of similar biomolecules such as ALT and histamine have been of interest in recent years [80,81].

Finally, histological analysis was used to evaluate possible toxic reactions and tumor inhibition effects of all treatment agents. In accordance with the IVIS images and the results of biochemical analysis, the histological findings showed that the tumor tissues in EGF-CAP groups were more suppressed compared to other groups with reductions in tumor sizes. In addition to these findings, the highest TUNEL immunoreactivity was elicited in the EGF-CAP group, indicating the induction of apoptotic cell death. Sha et al., (2020) showed that cell apoptosis was significantly increased with carboplatin in both *in vitro* and *in vivo* assays [82]. Overall, findings of histological analysis pointed out significant pathological changes occurring in liver and lung tissues. However, these changes decreased in EGF-CAP group. All these results suggest that the tumor inhibition effect of EGF-CAP administration was far superior to that of the carboplatin or CAP administration groups alone.

5. Conclusion

Receptor-mediated targeting of nanoparticles to lung adenocarcinoma represents a promising approach in cancer therapy. In this study, EGF was conjugated to alginate-PAMAM hybrid nanoparticles containing carboplatin for the treatment of non-small cell lung cancer tumors and EGF-CAP exerted the highest therapeutic potential in *in vivo* animal model. Indeed, the EGF-conjugated alginate-PAMAM nanoparticles offer several advantages, including increased drug stability, prolonged circulation time, and reduced side effects by minimizing exposure to healthy tissues. Targeting EGFR overexpressed on lung adenocarcinoma cells enhances the specificity of carboplatin delivery, potentially improving therapeutic outcomes. While this approach shows promise, during translation of the results to clinical setting, challenges may include potential off-target effects, mainly due to variations in EGFR expression among patients. In spite of that, receptor-mediated targeting of EGF-conjugated alginate-PAMAM nanoparticles to lung adenocarcinoma is a sophisticated strategy that holds potential for improving the precision and effectiveness of cancer therapy. However, ongoing research and clinical studies are essential to validate and optimize this approach for practical clinical applications.

Funding

This study was supported by Ege University, Scientific Research Foundation through FGA-2020-21665.

CRediT authorship contribution statement

Esra Ilhan-Ayisigi: Writing – original draft, Visualization, Validation, Methodology, Formal analysis, Data curation. **Pelin Saglam-Metiner:** Writing – original draft, Visualization, Validation, Methodology, Formal analysis, Data curation. **Ebru Sanci:** Visualization, Validation, Methodology, Data curation. **Buket Bakan:** Visualization, Validation, Methodology, Data curation. **Yeliz Yildirim:** Visualization, Validation, Formal analysis, Data curation. **Aylin Buhur:** Visualization, Validation, Formal analysis, Data curation. **Altug Yavasoglu:** Visualization, Validation, Supervision, Formal analysis, Data curation. **N. Ulku Karabay Yavasoglu:** Writing – review & editing, Supervision, Project administration, Methodology, Funding acquisition, Formal analysis,

Data curation. **Ozlem Yesil-Celiktas:** Writing – review & editing, Supervision, Resources, Project administration, Methodology, Investigation, Conceptualization.

Declaration of competing interest

On behalf of all authors, the corresponding author states that there is no conflict of interest.

Data availability

Data will be made available on request.

Appendix A. Supplementary data

Supplementary data to this article can be found online at https://doi.org/10.1016/j.ijbiomac.2024.129758.

References

[1] M.J. Mitchell, M.M. Billingsley, R.M. Haley, M.E. Wechsler, N.A. Peppas, R. Langer, Engineering precision nanoparticles for drug delivery, Nat. Rev. Drug Discov. 20 (2021) 101–124, https://doi.org/10.1038/s41573-020-0090-8.

[2] O. Afzal, A.S.A. Altamimi, M.S. Nadeem, S.I. Alzarea, W.H. Almalki, A. Tariq, B. Mubeen, B.N. Murtaza, S. Iftikhar, N. Riaz, I. Kazmi, Nanoparticles in drug delivery: from history to therapeutic applications, Nanomaterials 12 (2022) 4494, https://doi.org/10.3390/nano12244494.

[3] E. Ilhan-Ayisigi, G. Budak, M.S. Celiktas, C. Sevimli-Gur, O. Yesil-Celiktas, Anticancer activities of bioactive peptides derived from rice husk both in free and encapsulated form in chitosan, J. Ind. Eng. Chem. 103 (2021) 381–391, https://doi.org/10.1016/j.jiec.2021.08.006.

[4] S. Khizar, N. Zine, A. Errachid, N. Jaffrezic-Renault, A. Elaissari, Microfluidic-based nanoparticle synthesis and their potential applications, Electrophoresis 43 (2022) 819–838, https://doi.org/10.1002/elps.202100242.

[5] S. Bazban-Shotorbani, E. Dashtimoghadam, A. Karkhaneh, M.M. Hasani-Sadrabadi, K.I. Jacob, Microfluidic directed synthesis of alginate nanogels with tunable pore size for efficient protein delivery, Langmuir 32 (2016) 4996–5003, https://doi.org/10.1021/acs.langmuir.5b04645.

[6] S. Patil, K. Nune, R. Misra, Alginate/poly(amidoamine) injectable hybrid hydrogel for cell delivery, J. Biomater. Appl. 33 (2018) 295–314, https://doi.org/10.1177/0885328218790211.

[7] I. Matai, P. Gopinath, Chemically cross-linked hybrid nanogels of alginate and PAMAM dendrimers as efficient anticancer drug delivery vehicles, ACS Biomater. Sci. Eng. 2 (2016) 213–223, https://doi.org/10.1021/acsbiomaterials.5b00392.

[8] P.N. Nabi, N. Vahidfar, M.R. Tohidkia, A.A. Hamidi, Y. Omidi, A. Aghanejad, Mucin-1 conjugated polyamidoamine-based nanoparticles for image-guided delivery of gefitinib to breast cancer, Int. J. Biol. Macromol. 174 (2021) 185–197, https://doi.org/10.1016/j.ijbiomac.2021.01.170.

[9] R. Ali, M.K. Wendt, The paradoxical functions of EGFR during breast cancer progression, Signal. Transduct. Target. Ther. 2 (2017) 16042, https://doi.org/10.1038/sigtrans.2016.42.

[10] M. Sun, T. Wang, L. Li, X. Li, Y. Zhai, J. Zhang, W. Li, The application of inorganic nanoparticles in molecular targeted cancer therapy: EGFR targeting, Front. Pharmacol. 12 (2021), https://doi.org/10.3389/fphar.2021.702445.

[11] B. Foroughi-Nia, J. Barar, M.Y. Memar, A. Aghanejad, S. Davaran, Progresses in polymeric nanoparticles for delivery of tyrosine kinase inhibitors, Life Sci. 278 (2021) 119642, https://doi.org/10.1016/j.lfs.2021.119642.

[12] A.M. Master, S.A. Gupta, EGF receptor-targeted nanocarriers for enhanced cancer treatment, Nanomedicine 7 (2012) 1895–1906, https://doi.org/10.2217/nnm.12.160.

[13] A. Aghanejad, S.F. Bonab, M. Sepehri, F.S. Haghighi, A. Tarighatnia, C. Kreiter, N. D. Nader, M.R. Tohidkia, A review on targeting tumor microenvironment: the main paradigm shift in the mAb-based immunotherapy of solid tumors, Int. J. Biol. Macromol. 207 (2022) 592–610, https://doi.org/10.1016/j.ijbiomac.2022.03.057.

[14] X. She, L. Chen, L. Velleman, C. Li, C. He, J. Denman, T. Wang, S. Shigdar, W. Duan, L. Kong, The control of epidermal growth factor grafted on mesoporous silica nanoparticles for targeted delivery, J. Mater. Chem. B 3 (2015) 6094–6104, https://doi.org/10.1039/C5TB00790A.

[15] C.O. Silva, S.B. Petersen, C.P. Reis, P. Rijo, J. Molpeceres, A.S. Fernandes, O. Gonçalves, A.C. Gomes, I. Correia, H. Vorum, M.T. Neves-Petersen, EGF functionalized polymer-coated gold nanoparticles promote EGF photostability and EGFR internalization for photothermal therapy, PLoS One 11 (2016) 1–29, https://doi.org/10.1371/journal.pone.0165419.

[16] C. Tseng, T. Wang, G. Dong, S. Yuehhsıuwu, T. Young, M. Shıeh, P. Lou, F. Lin, Development of gelatin nanoparticles with biotinylated EGF conjugation for lung cancer targeting, Biomaterials 28 (2007) 3996–4005, https://doi.org/10.1016/j.biomaterials.2007.05.006.

[17] T. Shimada, M. Ueda, H. Jinno, N. Chiba, M. Wada, J. Watanabe, K. Ishihara, Y. Kitagawa, Development of targeted therapy with paclitaxel incorporated into EGF-conjugated nanoparticles, Anticancer Res. 29 (2009) 1009–1014. http://www.ncbi.nlm.nih.gov/pubmed/19414339.

[18] M.A. Sandoval, B.R. Sloat, D.S.P. Lansakara-P., A. Kumar, B.L. Rodriguez, K. Kiguchi, J. DiGiovanni, Z. Cui, EGFR-targeted stearoyl gemcitabine nanoparticles show enhanced anti-tumor activity, J. Control. Release 157 (2012) 287–296, https://doi.org/10.1016/j.jconrel.2011.08.015.

[19] B.P. Nikolaev, Y.Yu. Marchenko, L.Yu. Yakovleva, T.M. Zimina, A.V. Soloviev, V. V. Luchinin, A.V. Petrov, T.A. Scharafutdinova, A.V. Dobrodumov, Magnetic epidermal growth factor conjugate for targeted delivery to grafted tumor in mouse model, IEEE Trans. Magn. 49 (2013) 429–435, https://doi.org/10.1109/TMAG.2012.2223203.

[20] A.C. Marques, P.J. Costa, S. Velho, M.H. Amaral, Functionalizing nanoparticles with cancer-targeting antibodies: a comparison of strategies, J. Control. Release 320 (2020) 180–200, https://doi.org/10.1016/j.jconrel.2020.01.035.

[21] X.-H. Peng, Y. Wang, D. Huang, Y. Wang, H.J. Shin, Z. Chen, M.B. Spewak, H. Mao, X. Wang, Y. Wang, Z.G. Chen, S. Nie, D.M. Shin, Targeted delivery of cisplatin to lung cancer using ScFvEGFR-heparin-cisplatin nanoparticles, ACS Nano 5 (2011) 9480–9493, https://doi.org/10.1021/nn202410f.

[22] M. Talelli, C.J.F. Rijcken, S. Oliveira, R. van der Meel, P.M.P. van Bergen en Henegouwen, T. Lammers, C.F. van Nostrum, G. Storm, W.E. Hennink, Nanobody-shell functionalized thermosensitive core-crosslinked polymeric micelles for active drug targeting, J. Control. Release 153 (2011) 93–102, https://doi.org/10.1016/j.jconrel.2011.06.003.

[23] S. Yamamoto, J. Nakanism, Epidermal growth factor-gold nanoparticle conjugates-induced cellular responses: effect of interfacial parameters between cell and nanoparticle, Anal. Sci. 37 (2021) 741–745, https://doi.org/10.2116/analsci.20SCP16.

[24] B. Salama, C.-J. Chang, K. Kanehira, E.-S. El-Sherbini, G. El-Sayed, M. El-Adl, A. Taniguchi, EGF conjugation improves safety and uptake efficacy of titanium dioxide nanoparticles, Molecules 25 (2020) 4467, https://doi.org/10.3390/molecules25194467.

[25] H. Jin, J.F. Lovell, J. Chen, K. Ng, W. Cao, L. Ding, Z. Zhang, G. Zheng, Investigating the specific uptake of EGF-conjugated nanoparticles in lung cancer cells using fluorescence imaging, Cancer Nanotechnol. 1 (2010) 71–78, https://doi.org/10.1007/s12645-010-0009-x.

[26] Shevtsov, B. Nikolaev, L. Yakovleva, Y. Marchenko, A. Mikhrina, M. Martynova, O. Bystrova, A. Dobrodumov, A. Ischenko, I.V. Yakovenko, Superparamagnetic iron oxide nanoparticles conjugated with epidermal growth factor (SPION– EGF) for targeting brain tumors, Int. J. Nanomedicine (2014) 273, https://doi.org/10.2147/IJN.S55118.

[27] W. Kim, K.-Y. Na, K.-H. Lee, H.W. Lee, J.K. Lee, K.-T. Kim, Selective uptake of epidermal growth factor-conjugated gold nanoparticle (EGF-GNP) facilitates non-thermal plasma (NTP)-mediated cell death, Sci. Rep. 7 (2017) 10971, https://doi.org/10.1038/s41598-017-11292-z.

[28] A. Zhang, J. Nakanishi, Improved anti-cancer effect of epidermal growth factor-gold nanoparticle conjugates by protein orientation through site-specific mutagenesis, Sci. Technol. Adv. Mater. 22 (2021) 616–626, https://doi.org/10.1080/14686996.2021.1944783.

[29] S.H. Kiaie, S. Mojarad-Jabali, F. Khaleseh, S. Allahyari, E. Taheri, P. Zakeri-Milani, H. Valizadeh, Axial pharmaceutical properties of liposome in cancer therapy: recent advances and perspectives, Int. J. Pharm. 581 (2020) 119269, https://doi.org/10.1016/j.ijpharm.2020.119269.

[30] W.-W. Xu, D. Liu, Y. Cao, X. Wang, GE11 peptide-conjugated nanoliposomes to enhance the combinational therapeutic efficacy of docetaxel and siRNA in laryngeal cancers, Int. J. Nanomedicine 12 (2017) 6461–6470, https://doi.org/10.2147/IJN.S129946.

[31] S.J. Kang, H.Y. Jeong, M.W. Kim, I.H. Jeong, M.J. Choi, Y.M. You, C.S. Im, I. H. Song, T.S. Lee, Y.S. Park, Anti-EGFR lipid micellar nanoparticles co-encapsulating quantum dots and paclitaxel for tumor-targeted theranosis, Nanoscale 10 (2018) 19338–19350, https://doi.org/10.1039/C8NR05099F.

[32] E. da S. Santos, K.A.B. Nogueira, L.C.C. Fernandes, J.R.P. Martins, A.V.F. Reis, J. de B.V. Neto, I.J. da S. Júnior, C. Pessoa, R. Petrilli, J.O. Eloy, EGFR targeting for cancer therapy: pharmacology and immunoconjugates with drugs and nanoparticles, Int. J. Pharm. 592 (2021) 120082, https://doi.org/10.1016/j.ijpharm.2020.120082.

[33] E. Ilhan-Ayisigi, F. Ulucan, E. Saygili, P. Saglam-Metiner, S. Gulce-Iz, O. Yesil-Celiktas, Nano-vesicular formulation of propolis and cytotoxic effects in a 3D spheroid model of lung cancer, J. Sci. Food Agric. 100 (2020) 3525–3535, https://doi.org/10.1002/jsfa.10400.

[34] B. Aslanbay Guler, P. Saglam-Metiner, I. Deniz, Z. Demirel, O. Yesil-Celiktas, E. Imamoglu, Aligned with sustainable development goals: microwave extraction of astaxanthin from wet algae and selective cytotoxic effect of the extract on lung cancer cells, Prep. Biochem. Biotechnol. 53 (2023) 565–571, https://doi.org/10.1080/10826068.2022.2116455.

[35] A. International, ASTM International - ASTM F756-13 Standard Practice for Assessment of Hemolytic Properties of Materials, 2013.

[36] M.A. Dobrovolskaia, J.D. Clogston, B.W. Neun, J.B. Hall, A.K. Patri, S.E. McNeil, Method for analysis of nanoparticle hemolytic properties in vitro, Nano Lett. 8 (2008) 2180–2187, https://doi.org/10.1021/nl0805615.

[37] M. Zimmermann, Ethical guidelines for investigations of experimental pain in conscious animals, Pain 16 (1983) 109–110, https://doi.org/10.1016/0304-3959(83)90201-4.

[38] H. Song, F. Quan, Z. Yu, M. Zheng, Y. Ma, H. Xiao, F. Ding, Carboplatin prodrug conjugated Fe3O4 nanoparticles for magnetically targeted drug delivery in ovarian cancer cells, J. Mater. Chem. B 7 (2019) 433–442, https://doi.org/10.1039/C8TB02574F.

[39] K. Birgül, Y. Yıldırım, H.Y. Karasulu, E. Karasulu, A.I. Uba, K. Yelekçi, H. Bekçi, A. Cumaoğlu, L. Kabasakal, Ö. Yılmaz, Ş.G. Küçükgüzel, Synthesis, molecular modeling, in vivo study and anticancer activity against prostate cancer of (+) (S)-naproxen derivatives, Eur. J. Med. Chem. 208 (2020) 112841, https://doi.org/10.1016/j.ejmech.2020.112841.
[40] G. Yigitturk, A.C. Acara, O. Erbas, F. Oltulu, N.U.K. Yavasoglu, A. Uysal, A. Yavasoglu, The antioxidant role of agomelatine and gallic acid on oxidative stress in STZ induced type I diabetic rat testes, Biomed. Pharmacother. 87 (2017) 240–246, https://doi.org/10.1016/j.biopha.2016.12.102.
[41] D. Bolat, F. Oltulu, A. Uysal, T. Kose, B. Gunlusoy, G. Yigitturk, N.S. Turk, T. Turan, Effects of losartan on experimental varicocele-induced testicular germ cell apoptosis, Andrologia 48 (2016) 840–846, https://doi.org/10.1111/and.12638.
[42] Y. Zhang, X. Liu, L. Li, Z. Guo, Z. Xue, X. Lu, An electrochemical paracetamol sensor based on layer-by-layer covalent attachment of MWCNTs and a G4.0 PAMAM modified GCE, Anal. Methods 8 (2016) 2218–2225, https://doi.org/10.1039/C5AY03241E.
[43] W.F. Loeb, F. Quimby, The Clinical Chemistry of Laboratory Animals, CRC Press, Second Edi, 1999.
[44] T. Sadhukha, S. Prabha, Encapsulation in nanoparticles improves anti-cancer efficacy of carboplatin, AAPS PharmSciTech 15 (2014) 1029–1038, https://doi.org/10.1208/s12249-014-0139-2.
[45] F. Griesinger, E.E. Korol, S. Kayaniyil, N. Varol, T. Ebner, S.M. Goring, Efficacy and safety of first-line carboplatin-versus cisplatin-based chemotherapy for non-small cell lung cancer: a meta-analysis, Lung Cancer 135 (2019) 196–204, https://doi.org/10.1016/j.lungcan.2019.07.010.
[46] G.J. Kirkpatrick, J.A. Plumb, O.B. Sutcliffe, D.J. Flint, N.J. Wheate, Evaluation of anionic half generation 3.5–6.5 poly(amidoamine) dendrimers as delivery vehicles for the active component of the anticancer drug cisplatin, J. Inorg. Biochem. 105 (2011) 1115–1122, https://doi.org/10.1016/j.jinorgbio.2011.05.017.
[47] D. Kalita, D. Shome, V.G. Jain, K. Chadha, J.R. Bellare, In vivo intraocular distribution and safety of periocular nanoparticle carboplatin for treatment of advanced retinoblastoma in humans, Am J. Ophthalmol. 157 (2014) 1109–1115, https://doi.org/10.1016/j.ajo.2014.01.027.
[48] Z. Fu, S. Li, S. Han, C. Shi, Y. Zhang, Antibody drug conjugate: the "biological missile" for targeted cancer therapy, Signal. Transduct. Target. Ther. 7 (2022) 93, https://doi.org/10.1038/s41392-022-00947-7.
[49] S. Jin, Y. Sun, X. Liang, X. Gu, J. Ning, Y. Xu, S. Chen, L. Pan, Emerging new therapeutic antibody derivatives for cancer treatment, Signal. Transduct. Target. Ther. 7 (2022) 39, https://doi.org/10.1038/s41392-021-00868-x.
[50] E. Saygili, E. Kaya, E. Ilhan-Ayisigi, P. Saglam-Metiner, E. Alarcin, A. Kazan, E. Girgic, Y.-W. Kim, K. Gunes, G.G. Eren-Ozcan, D. Akakin, J.-Y. Sun, O. Yesil-Celiktas, An alginate-poly(acrylamide) hydrogel with TGF-β3 loaded nanoparticles for cartilage repair: biodegradability, biocompatibility and protein adsorption, Int. J. Biol. Macromol. 172 (2021) 381–393, https://doi.org/10.1016/j.ijbiomac.2021.01.069.
[51] O. Yesil-Celiktas, C. Pala, E.O. Cetin-Uyanikgil, C. Sevimli-Gur, Synthesis of silica-PAMAM dendrimer nanoparticles as promising carriers in Neuro blastoma cells, Anal. Biochem. 519 (2017) 1–7, https://doi.org/10.1016/j.ab.2016.12.004.
[52] A. Yaghmur, A. Ghazal, R. Ghazal, M. Dimaki, W.E. Svendsen, A hydrodynamic flow focusing microfluidic device for the continuous production of hexosomes based on docosahexaenoic acid monoglyceride, Phys. Chem. Chem. Phys. 21 (2019) 13005–13013, https://doi.org/10.1039/c9cp02393c.
[53] C.B. Roces, D. Christensen, Y. Perrie, Translating the fabrication of protein-loaded poly(lactic-co-glycolic acid) nanoparticles from bench to scale-independent production using microfluidics, Drug Deliv. Transl. Res. 10 (2020) 582–593, https://doi.org/10.1007/s13346-019-00699-y.
[54] E. Ilhan-Ayisigi, B. Yaldiz, G. Bor, A. Yaghmur, O. Yesil-Celiktas, Advances in microfluidic synthesis and coupling with synchrotron SAXS for continuous production and real-time structural characterization of nano-self-assemblies, Colloids Surf. B 201 (2021) 111633, https://doi.org/10.1016/j.colsurfb.2021.111633.
[55] E. Alarçin, A. Bal-ozturk, Development and Characterization of Oxaceprol-loaded Poly-lactide-co-glycolide Nanoparticles for the Treatment of Osteoarthritis, 2020, pp. 1–10, https://doi.org/10.1002/ddr.21642.
[56] N. Othman, M.J. Masarudin, C.Y. Kuen, N.A. Dasuan, L.C. Abdullah, S.N.A. M. Jamil, Synthesis and optimization of chitosan nanoparticles loaded with l-ascorbic acid and thymoquinone, Nanomaterials 8 (2018) 820, https://doi.org/10.3390/nano8110920.
[57] R. Praveen, P.R.P. Verma, S.K. Singh, J.K. George, Cross linked alginate gel beads as floating drug delivery system for cefdinir: optimization using Box–Behnken design, J. Pharm. Investig. 45 (2015) 187–199, https://doi.org/10.1007/s40005-014-0164-x.
[58] H.J. Lee, G.M. Fernandes-Cunha, I. Putra, W.-G. Koh, D. Myung, Tethering growth factors to collagen surfaces using copper-free click chemistry: surface characterization and in vitro biological response, ACS Appl. Mater. Interfaces 9 (2017) 23389–23399, https://doi.org/10.1021/acsami.7b05262.
[59] C. Kececiler-Emir, E. Ilhan-Ayisigi, C. Celen-Erden, A. Nalbantsoy, O. Yesil-Celiktas, Synthesis of resveratrol loaded hybrid silica-PAMAM dendrimer nanoparticles with emphases on inducible nitric oxide synthase and cytotoxicity, Plant Foods Hum. Nutr. 76 (2021) 219–225, https://doi.org/10.1007/s11130-021-00897-5.
[60] L. Zhang, Q. Chen, Y. Ma, J. Sun, Microfluidic methods for fabrication and engineering of nanoparticle drug delivery systems, ACS Appl. Bio Mater. 3 (2020) 107–120, https://doi.org/10.1021/acsabm.9b00853.
[61] P. Saglam-Metiner, S. Gulce-Iz, C. Biray-Avci, Bioengineering-inspired three-dimensional culture systems: organoids to create tumor microenvironment, Gene 686 (2019) 203–212, https://doi.org/10.1016/j.gene.2018.11.058.
[62] E. Yildiz-Ozturk, P. Saglam-Metiner, O. Yesil-Celiktas, Lung carcinoma spheroids embedded in a microfluidic platform, Cytotechnology 73 (2021) 457–471, https://doi.org/10.1007/s10616-021-00470-7.
[63] H. Eguchi, R. Akizuki, R. Maruhashi, M. Tsukimoto, T. Furuta, T. Matsunaga, S. Endo, A. Ikari, Increase in resistance to anticancer drugs involves occludin in spheroid culture model of lung adenocarcinoma A549 cells, Sci. Rep. 8 (2018) 15157, https://doi.org/10.1038/s41598-018-33566-w.
[64] H. Hashemzadeh, A.H.A. Kelkawi, A. Allahverdi, M. Rothbauer, P. Ertl, H. Naderi-Manesh, Fingerprinting metabolic activity and tissue integrity of 3D lung cancer spheroids under gold nanowire treatment, Cells 11 (2022) 478, https://doi.org/10.3390/cells11030478.
[65] L.M. Bareford, P.W. Swaan, Endocytic mechanisms for targeted drug delivery, Adv. Drug Deliv. Rev. 59 (2007) 748–758, https://doi.org/10.1016/j.addr.2007.06.008.
[66] U. Cavallaro, G. Christofori, Multitasking in tumor progression: signaling functions of cell adhesion molecules, Ann. N. Y. Acad. Sci. 1014 (2004) 58–66, https://doi.org/10.1196/annals.1294.006.
[67] H. Xu, Y. Yu, D. Marciniak, A.K. Rishi, F.H. Sarkar, O. Kucuk, A.P.N. Majumdar, Epidermal growth factor receptor (EGFR)–related protein inhibits multiple members of the EGFR family in colon and breast cancer cells, Mol. Cancer Ther. 4 (2005) 435–442, https://doi.org/10.1158/1535-7163.MCT-04-0280.
[68] A. Onaciu, R. Munteanu, V.C. Munteanu, D. Gulei, L. Raduly, R.-I. Feder, R. Pirlog, A.G. Atanasov, S.S. Korban, A. Irimie, I. Berindan-Neagoe, Spontaneous and induced animal models for cancer research, Diagnostics 10 (2020) 660, https://doi.org/10.3390/diagnostics10090660.
[69] Z. Li, W. Zheng, H. Wang, Y. Cheng, Y. Fang, F. Wu, G. Sun, G. Sun, C. Lv, B. Hui, Application of animal models in cancer research: recent progress and future prospects, Cancer Manag. Res. 13 (2021) 2455–2475, https://doi.org/10.2147/CMAR.S302565.
[70] A.R. Afshari, M. Sanati, H. Mollazadeh, P. Kesharwani, T.P. Johnston, A. Sahebkar, Nanoparticle-based drug delivery systems in cancer: a focus on inflammatory pathways, Semin. Cancer Biol. 86 (2022) 860–872, https://doi.org/10.1016/j.semcancer.2022.01.008.
[71] Z. Zhang, J. Chen, L. Ding, H. Jin, J.F. Lovell, I.R. Corbin, W. Cao, P. Lo, M. Yang, M. Tsao, Q. Luo, G. Zheng, HDL-mimicking peptide–lipid nanoparticles with improved tumor targeting, Small 6 (2010) 430–437, https://doi.org/10.1002/smll.200901515.
[72] W. Zhang, C. Li, C. Shen, Y. Liu, X. Zhao, Y. Liu, D. Zou, Z. Gao, C. Yue, Prodrug-based nano-drug delivery system for co-encapsulate paclitaxel and carboplatin for lung cancer treatment, Drug Deliv. 23 (2016) 2575–2580, https://doi.org/10.3109/10717544.2015.1035466.
[73] G. Silva-Santana, J.C. Bax, D.C.S. Fernandes, D.T.L. Bacellar, C. Hooper, A.A.S. O. Dias, C.B. Silva, A.M. de Souza, S. Ramos, R.A. Santos, T.R. Pinto, M.A. Ramão, A.L. Mattos-Guaraldi, Clinical hematological and biochemical parameters in Swiss, BALB/c, C57BL/6 and B6D2F1 Mus musculus, Animal Model. Exp. Med. 3 (2020) 304–315, https://doi.org/10.1002/ame2.12139.
[74] R. Ravel, Clinical Laboratory Medicine: Clinical Applications of Laboratory Data, 6th Editio, Mosby, 1995.
[75] C. Grimm, G. Hofstetter, S. Aust, I. Mutz-Dehbalaie, M. Bruch, G. Heinze, J. Rahhal-Schupp, A. Reinthaller, N. Concin, S. Polteraue, Association of gamma-glutamyltransferase with severity of disease at diagnosis and prognosis of ovarian cancer, Br. J. Cancer 109 (2013) 610–614, https://doi.org/10.1038/bjc.2013.323.
[76] M.H. Hanigan, B.C. Gallagher, D.M. Townsend, V. Gabarra, γ-glutamyl transpeptidase accelerates tumor growth and increases the resistance of tumors to cisplatin in vivo, Carcinogenesis 20 (1999) 553–559, https://doi.org/10.1093/carcin/20.4.553.
[77] B.C. Fuchs, Y. Hoshida, T. Fujii, L. Wei, S. Yamada, G.Y. Lauwers, C.M. McGinn, D. K. DePeralta, X. Chen, T. Kuroda, M. Lanuti, A.D. Schmitt, S. Gupta, A. Crenshaw, R. Onofrio, B. Taylor, W. Winckler, N. Bardeesy, P. Caravan, T.R. Golub, K. K. Tanabe, Epidermal growth factor receptor inhibition attenuates liver fibrosis and development of hepatocellular carcinoma, Hepatology 59 (2014) 1577–1590, https://doi.org/10.1002/hep.26898.
[78] A. Natarajan, B. Wagner, M. Sibilia, The EGF receptor is required for efficient liver regeneration, Proc. Natl. Acad. Sci. 104 (2007) 17081–17086, https://doi.org/10.1073/pnas.0704126104.
[79] G.D. Girnun, L. Chen, J. Silvaggi, R. Drapkin, L.R. Chirieac, R.F. Padera, R. Upadhyay, S.B. Vafai, R. Weissleder, U. Mahmood, E. Naseri, S. Buckley, D. Li, J. Force, K. McNamara, G. Demetri, B.M. Spiegelman, K.-K. Wong, Regression of drug-resistant lung cancer by the combination of rosiglitazone and carboplatin, Clin. Cancer Res. 14 (2008) 6478–6486, https://doi.org/10.1158/1078-0432.CCR-08-1128.
[80] R. Singh, Z. Wang, C. Marques, R. Min, B. Zhang, S. Kumar, Alanine aminotransferase detection using TIT assisted four tapered fiber structure-based LSPR sensor: from healthcare to marine life, Biosens. Bioelectron. 236 (2023) 115424, https://doi.org/10.1016/j.bios.2023.115424.
[81] W. Zhang, R. Singh, Z. Wang, G. Li, Y. Xie, R. Jha, C. Marques, B. Zhang, S. Kumar, Humanoid shaped optical fiber plasmon biosensor functionalized with graphene oxide/multi-walled carbon nanotubes for histamine detection, Opt. Express 31 (2023) 11788–11803, https://doi.org/10.1364/OE.486844.
[82] J. Sha, D. Cao, R. Cui, L. Xia, X. Hua, Y. Lu, S. Han, Mannose impairs lung adenocarcinoma growth and enhances the sensitivity of A549 cells to carboplatin, Cancer Manag. Res. 12 (2020) 11077–11083, https://doi.org/10.2147/CMAR.S278673.